

NRL Report 8367
EOTPO Report No. 57

Passive Infrared Surveillance, Part II: Threshold-Crossing Receivers

RICHARD A. STEINBERG

Electro-Optical Technology Program Office (EOTPO)

January 24, 1980



**ELECTRO-OPTICAL TECHNOLOGY PROGRAM OFFICE
NAVAL RESEARCH LABORATORY
Washington, D.C. 20375**

Approved for public release; distribution unlimited.

Reviewed and approved by:
Dr. John M. MacCallum, Jr.
Head, Electro-Optical Technology Program Office

SECURITY CLASSIFICATION OF THIS PAGE (When Data Entered)

REPORT DOCUMENTATION PAGE		READ INSTRUCTIONS BEFORE COMPLETING FORM
1. REPORT NUMBER NRL Report 8367	2. GOVT ACCESSION NO.	3. RECIPIENT'S CATALOG NUMBER
4. TITLE (and Subtitle) PASSIVE INFRARED SURVEILLANCE, PART II: THRESHOLD-CROSSING RECEIVERS		5. TYPE OF REPORT & PERIOD COVERED Interim report on a continuing NRL problem
		6. PERFORMING ORG. REPORT NUMBER EOTPO Report 57
7. AUTHOR(s) Richard A. Steinberg		8. CONTRACT OR GRANT NUMBER(s)
9. PERFORMING ORGANIZATION NAME AND ADDRESS Naval Research Laboratory Washington, D.C. 20375		10. PROGRAM ELEMENT, PROJECT, TASK AREA & WORK UNIT NUMBERS NRL Problem N01-29
11. CONTROLLING OFFICE NAME AND ADDRESS		12. REPORT DATE January 24, 1980
		13. NUMBER OF PAGES 59
14. MONITORING AGENCY NAME & ADDRESS (if different from Controlling Office)		15. SECURITY CLASS. (of this report) UNCLASSIFIED
		15a. DECLASSIFICATION/DOWNGRADING SCHEDULE
16. DISTRIBUTION STATEMENT (of this Report) Approved for public release; distribution unlimited.		
17. DISTRIBUTION STATEMENT (of the abstract entered in Block 20, if different from Report)		
18. SUPPLEMENTARY NOTES		
19. KEY WORDS (Continue on reverse side if necessary and identify by block number) Infrared technology Electro-Optical Technology Program Office (EOTPO) Electro-optics Surveillance		
20. ABSTRACT (Continue on reverse side if necessary and identify by block number) A number of infrared passive surveillance receivers are analyzed with the theory developed in Part I (NRL Report 8320). The specific problem of interest is the detection of low-contrast point-source targets against high-contrast structured backgrounds. A new and promising approach to signal processing is proposed for minimizing background-induced false alarms while retaining maximum target-detection sensitivity. It is shown that improvements in focal-plane-array (FPA) technology employing time delay and integration (TDI) may afford "excess" detector sensitivity that can be intentionally sacrificed in the interest of enhanced performance against structured scenes.		

CONTENTS

GLOSSARY OF SYMBOLS	v
INTRODUCTION	1
BACKGROUND	3
Concepts and Definitions	3
Current Statistics	6
Threshold-Crossing Rates	9
Mean-Crossing Times and Times of Closest Approach	10
Fixed-Threshold Processors	11
Initial Assessment of Adaptive Vs Fixed-Threshold Processors	12
Uniform Scenes of Known Brightness	14
Uniform-Background False-Alarm Penalty	14
Time Delay and Integration	15
Ideal (CFAR) Adaptive-Threshold Receivers	15
Mean Video Estimators	17
UNIFORM SCENES OF UNKNOWN BRIGHTNESS	18
Fixed-Threshold Processors	19
Adaptive-Threshold Processors	19
STRUCTURED SCENES	22
Slowly Varying Scenes	22
Model Filters and Backgrounds	24
Figure 6 Processor	26
Improved Processors	27
Noise Bandwidth and Dwell Time	33
The Promise of Focal-Plane-Array Technology	35

APPENDIX A.—Calculating the Average Current from Background Data	37
APPENDIX B—Efficient Estimators for Nonstationary Shot Noise	40
APPENDIX C—Square Root of a Gaussian Random Process	47
REFERENCES	51

GLOSSARY OF SYMBOLS

Symbol	Definition
$A(t)$	Eq. (C9) A Gaussian random process (generally nonstationary)
A_{det}	Eq. (A3) Detector active area
AT	Adaptive threshold
$B(t)$	Eq. (C9) Square root of a Gaussian random process
BLIP	Background (quantum noise) limited photodetector
BSI	Background-structure-induced fluctuations in the ensemble-average video signal
BSL	Background-structure limited (performance regime)
C	Eq. (74b) Ratio of noise variance to scene radiance
CFAR	Constant false-alarm rate (performance regime)
d	Eq. (A6) Focal length of optics [cm]
e	Eq. (16) Electronic charge [C]
$E\{\cdot\}$	Eq. (2) Statistical expectation operator (ensemble average)
ESN	Efficient shot-noise estimator (for the rms value of nonstationary shot noise)
f	Eq. (11) Electrical frequency [Hz]
$f^{\#}$	Eq. (A4) Optical focal-length ratio
\mathbf{f}	Eq. (A6) Two-dimensional vector spatial frequency
f_A	Eq. (C7) Probability density function of $A(t)$
$f_{\hat{\sigma}_Y \sigma_Y}$	Eq. (B41) Probability density function of $\hat{\sigma}_Y$ conditioned on σ_Y
FAP	Eq. (52) False-alarm penalty
FAR	Eq. (8) False-alarm rate

FPA		Focal-plane array
FT		Fixed threshold
$h(t)$	Eq. (11)	Impulse response of the postdetector electrical filter
$\dot{h}(t)$	Eq. (17)	Time derivative of $h(t)$
$H(f)$	Eq. (11)	Transfer function of the postdetector filter; Fourier transform of $h(t)$
$h_0(t)$	Eq. (31)	Impulse response of the threshold filter
$H_0(f)$	Eq. (B20)	Fourier transform of $h_0(t)$
I_i	Eq. (4)	Subinterval of the time interval I_0
I_0	Eq. (3)	An interval of time
IRST		Infrared search and track
J	Eq. (2)	Number of threshold crossings (an integer random variable)
K		Threshold-gain constant
K_0	Eq. (A4)	Ratio of the focal-plane irradiance to the scene radiance
m_A	Eq. (C1)	Expected value of $A(t)$
m_B	Eq. (C1)	Expected value of $B(t)$
m_E	Eq. (A4)	Expected value of the focal-plane irradiance
m_J	Eq. (2)	Expected value of the crossing count
\dot{m}_J	Eq. (3)	Threshold-crossing rate (the time derivative of m_J)
\dot{m}_{J_0}	Eq. (36)	Rate of positive-slope zero crossings
m_L	Eq. (74a)	Scene spatial radiance distribution
$m_{\mathcal{L}}(\mathbf{f})$	Eq. (A8)	Two-dimensional spatial Fourier transform of $m_L(\mathbf{r})$
m_Q	Eq. (A2)	Mean photon flux incident on a photodetector
m_X	Eq. (9)	Expected value of the unfiltered current $X(t)$
m_Y	Eq. (12)	Expected value of the video signal $Y(t)$

$m_{\dot{Y}}$	Eq. (13)	Expected value of $\dot{Y}(t)$
m_Y^{\pm}	Eq. (147b)	Time-advanced and time-delayed versions of $m_Y(t)$
\hat{m}_Y	Eq. (60)	Estimate for m_Y
$m_{\hat{m}_Y}$	Eq. (61)	Expected value of \hat{m}_Y
$m_{\hat{\sigma}_Y}$	Eq. (B29)	Expected value of $\hat{\sigma}_Y$
M	Eq. (151)	Noise bandwidth parameter of the postdetector electrical filter
MTF	Eq. (A6)	Modulation transfer function
N	Eq. (58)	Number of series TDI detectors
NEI		Noise-equivalent irradiance
$P(\mathbf{r})$	Eq. (A7)	"Pupil function" of a focal-plane detector
$\mathcal{P}(\mathbf{f})$	Eq. (A7)	Two-dimensional spatial Fourier transform of $P(\mathbf{r})$
P_D	Eq. (6)	Probability of detection
P_{FA}	Eq. (7)	False-alarm probability
QNL		Quantum-noise limited (performance regime)
\mathbf{r}	Eq. (A7)	Two-dimensional focal-plane location vector
R_I	Eq. (A5)	Photodetector current responsivity [$\text{A}\cdot\text{W}^{-1}$]
$\text{rect}(\cdot)$	Eq. (B9)	"Rectangle function" depicted in Fig. B3
$\text{sinc}(\cdot)$	Eq. (B11)	Fourier transform of $\text{rect}(\cdot)$
t	Eq. (3)	Time
t_{ca}	Eq. (44)	Time of closest approach
t_{mc}	Eq. (42)	Mean-crossing time
t_{TC}	Eq. (1)	Threshold-crossing time (a random variable)
T_d	Eq. (31)	Delay time; sensor dwell time

$T(I_0)$	Eq. (8)	Duration of time interval I_0 [s]
T_F	Eq. (A6)	System frame time [s]
TDI		Time delay and integration
u	Eq. (39)	Normalized mean threshold level
\mathbf{v}	Eq. (A6)	Focal-plane scan velocity
$W(k)$	Eq. (B8)	Time-sampled version of $Y(t)$
x_0	Eq. (115)	Dc component of the detected photocurrent, in the absence of an object in the sensor's field of view [A]
x_1	Eq. (115)	Peak contrast of an object against its background [dimensionless]
$X(t)$	Eq. (9)	Unfiltered photocurrent [A]
$Y(t)$	Eq. (10)	Filtered photocurrent [A]
y_0	Eq. (47)	Sample function of Y_0
$Y_0(t)$	Eq. (31)	Threshold current [A]
α	Eq. (54)	Ratio of noise bandwidths
$\partial_{\sigma_Y, \sigma_Y}^2$	Eq. (B40)	Second partial derivative with respect to σ_Y
Δf	Eq. (25)	Noise bandwidth of $H(f)$
Δf_0	Eq. (54)	Noise bandwidth of $H_0(f)$
$(\Delta f)_{rms}$	Eq. (48)	Rms bandwidth of $H(f)$
Δm_J	Eq. (4)	Increment in m_J
ϵ	Eq. (B27)	Relative mean estimation error for σ_Y
$\epsilon_{\hat{m}_Y}$	Eq. (63)	Relative mean estimation error for m_Y
$\epsilon_{\hat{\sigma}_Y}$	Eq. (64)	Relative mean estimation error for σ_Y
η	Eq. (A2)	Detector quantum efficiency
$\mu(\cdot)$	Eq. (B41)	Unit step function

σ_A	Eq. (C2)	Standard deviation of $A(t)$
σ_B	Eq. (C11)	Standard deviation of $B(t)$
σ_{CRLB}	Eq. (B40)	Cramér-Rao lower bound for $\sigma_{\hat{\sigma}_Y}$
σ_Y	Eq. (14)	Standard deviation of $Y(t)$
$\sigma_{\dot{Y}}$	Eq. (15)	Standard deviation of $\dot{Y}(t)$
σ_{YY_0}	Eq. (37)	Root-sum-square of σ_Y and σ_{Y_0}
$\sigma_{\dot{Y}\dot{Y}_0}$	Eq. (38)	Root-sum-square of $\sigma_{\dot{Y}}$ and $\sigma_{\dot{Y}_0}$
$\hat{\sigma}_Y$	Eq. (60)	Estimate for σ_Y
σ_Y^{\pm}	Eq. (147a)	Time-advanced and time-delayed versions of $\sigma_Y(t)$
$\sigma_{\hat{\sigma}_Y}$	Eq. (B4)	Root-mean-square estimation error for σ_Y
τ	Eq. (115)	Half-width at half-maximum of an object in the sensor's field of view [s]
τ_o	Eq. (A4)	Transmittance of the optical train
$\phi(\cdot)$	Eq. (B42)	Normalized Gaussian density function
χ	Eq. (65)	Ratio of m_Y to σ_{YY_0}
\otimes	Eq. (10)	Convolution operator

PASSIVE INFRARED SURVEILLANCE, PART II: THRESHOLD-CROSSING RECEIVERS

INTRODUCTION

The objective of an infrared surveillance receiver is to passively detect targets at long range while keeping false alarms acceptably infrequent. In this report we begin with a review of the surveillance-receiver analysis model developed in Part I [1], which relates expected system performance to appropriate descriptions of the background scene, the electro-optic sensor, and the structure of the signal processor. We then apply the principles elucidated in Part I to the processor design problem. Some of the ideas underlying the approach and some of the main results are summarized below.

The signal processor must examine the preamplifier output waveform and classify it either as targetlike or backgroundlike in structure, according to a set of criteria chosen by the system designer. Since the structure of the time variations in the video signal figures so importantly in how well the processor performs, we now discuss the mechanisms that give rise to these time variations.

The video waveform at the output of the postdetector filter of a scanning background-limited (BLIP) photodetector displays fluctuations having two fundamentally different origins:

- Quantum noise. Time-of-arrival fluctuations of the individual photons incident on the detector cause random variations in the photosignal called quantum noise or photon noise.
- Background-structure-induced fluctuations. Scanning the sensor across spatial variations in the scene radiance induces time variations in the photosignal referred to as background-structure-induced (BSI) fluctuations.

Each of these two basic mechanisms enters into the statistical representation of the video signal in complementary, but distinctly different, ways.

The background-structure-induced fluctuations enter into the statistical description of the video signal as a modulation imposed on the mean value of the video. Photon noise enters into the statistical representation of the video as the origin of the variance of the video about its mean. The statistical characterization is complete once the time-varying mean and variance of the video signal are specified, since the video is a nonstationary Gaussian random process.*

Manuscript submitted September 14, 1979.

*This fundamental description of the video-signal statistics has apparently not been previously applied to the passive-surveillance problem. Validity of the nonstationary Gaussian model for the video is assured whenever the expected number of photons incident on the detector during a sensor dwell time is much greater than unity [2].

Each of the candidate processor designs we describe in this report consists of two parts: one part for estimating the mean video signal (as determined by the background structure), and a second part for estimating the noise variance due to quantum noise. A main result in this report is the proposal of a new signal-processor structure for generating high-confidence estimates of the time-varying rms quantum noise. Implementation of the proposed quantum-noise estimator requires a sensor with either true dc response or synthetic dc restoration.

The second main component of the signal processor, the mean-video estimator, has a more critical impact on system performance than the quantum-noise estimator when operating against highly structured scenes. Unfortunately, the mean-video estimator is also more difficult to design, since the designer is required to make assumptions regarding the nature of the structured background.

We concentrate our discussion of mean-video estimators on three types of linear filters, evaluating their performance against a succession of increasingly complex model backgrounds:

- uniform scenes of known radiance,
- uniform scenes of unknown radiance,
- slowly varying nonuniform scenes, and
- scenes containing objects of arbitrary contrast and size.*

Improved mean-video estimators can no doubt be developed by incorporating actual measured background scenes into the processor-design-and-evaluation procedure and by expanding the scope of candidate processor designs to include nonlinear algorithms as well as linear ones [3]. Although a representative database of distributions of measured background infrared radiance is thus required both for designing and assessing more advanced processor algorithms, we do not consider the availability of such data in this report.

In addition to the limited scope of our model backgrounds and mean-video-estimation algorithms, a number of implicit assumptions underlie the approach to receiver design outlined above. Perhaps foremost of these is the basically deterministic nature of our model backgrounds. For example, the only requirement on each member of the class of "slowly varying" structured backgrounds is that the relative change in radiance from one sensor dwell time to the next be much smaller than unity. We make no attempt to give a statistical description, such as a probability density or correlation function, either to individual scenes or to the ensemble of scenes.

The utility of the "unknown but nonrandom" infrared-background representation is rationalized by paraphrasing Van Trees [4, p. 456] (with the words in brackets modifying the original text):

"It is sometimes unrealistic to consider the signal ... as a random waveform. For example, we may know that each time a [false alarm] occurs the [background scene] will have certain distinctive features. If the [background] is

*This final category of model backgrounds subsumes the class of real backgrounds containing point objects (such as targets) of either positive or negative contrast.

modeled as a sample function of a random process ... we may average out the features that are important ... Here it is more useful to model the [background] as an unknown, but nonrandom, waveform."

The spatial correlation function (or its Fourier transform, the Wiener spectrum) is an example of a statistical scene description that illustrates this point. Typically, the presence or absence of a point target in a given scene has a dominant effect on system performance while having a negligible effect on the correlation function of a large, structured scene.

Since we require a deterministic description for the background spatial variations, we sometimes refer to our performance model and our performance assessments as background conditional. Another implicit assumption in our design procedure concerns the restricted nature of the target/background discriminant that we use.

Of all the possible target/background discriminants, such as radiance variations with time*, space, polarization, and spectral content, we will consider only the spatial discriminant. Moreover we will make no attempt to exploit the spatial character of backgrounds. Any attempt to do so is complicated by the enormous diversity of structure displayed by natural scenes. Instead we will key on the known point character of the target. Each time we propose a candidate processing structure, we will ask the same question: Are there any nonpointlike structural features that could induce a threshold crossing? If so, the signal processor will be modified in a way intended to correct the apparent deficiency. Our ultimate objective is to construct a receiver that is sensitive only to the presence of pointlike objects in the sensor's field of view.

At present the limiting effect on system performance is generally background structure rather than detector sensitivity. Thus improvements in detector sensitivity are of little use, unless we can trade off sensitivity for improved performance against structured scenes.

In the final part of this report we will examine the usual search-set rule of thumb relating electrical bandwidth and sensor dwell time. We will find that the use of large video bandwidths, in violation of the rule of thumb, enables us to sacrifice some degree of performance against uniform backgrounds in the interest of enhanced performance against nonuniform backgrounds. Fortunately the performance degradation thus incurred against uniform scenes can be offset by means of focal-plane detector arrays (FPA) employing time-delay-and-integration (TDI) logic. Thus, we will establish a concrete link between advancements in component technology and overall system performance.

BACKGROUND

Concepts and Definitions

The two conventional parameters for measuring how well the infrared search-and-track (IRST) sensor accomplishes its dual objectives of target detection and false-target rejection are the probability of target detection (P_D) and the false-alarm rate (FAR).

*For example, tracking algorithms are neither modeled nor discussed, even though they may play an important role in target/background discrimination as well as target tracking [5].

TheIRST performance model described below [1] requires as input complete descriptions of theIRST sensor and the scene radiance distribution (possibly including a target). As output the model generates the probability that theIRST device declares (rightly or wrongly) a target's presence in the scene. *A priori* knowledge as to whether a target was in fact present in the specified scene allows interpretation of the target declaration probability (m_j) either as a target-detection probability (P_D) or as a false-alarm probability (P_{FA}).

Photon fluctuation noise is the only stochastic aspect of the model; the background must be specified as a radiance map of arbitrary, but deterministic structure. Thus the performance predictions made with this model are background conditional.

TheIRST analysis model that follows applies to threshold-comparison receivers configured as in Fig. 1. The current $X(t)$ at the output of the detector is input to an electrical filter of transfer function $H(f)$. The output current $Y(t)$ of the electrical filter is compared with a threshold $Y_0(t)$. If $Y(t)$ exceeds the threshold, the presence of a target is declared; otherwise no target declaration is made.

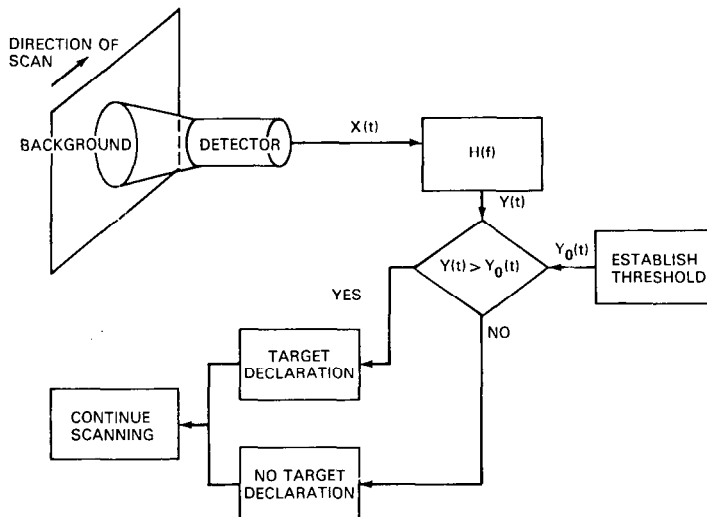


Fig. 1 — A basic threshold-comparison receiver. The photodetector in this figure is idealized in that it is presumed to have a perfect all-pass electrical frequency characteristic; the frequency-dependent part of the detector responsivity is lumped together with the transfer function of the postdetector filter to obtain $H(f)$. A target declaration is made whenever the filtered current $Y(t)$ exceeds the threshold level $Y_0(t)$.

Figure 1 suggests that the threshold-establishing mechanism should suppress clutter-induced threshold crossings (false alarms) by increasing $Y_0(t)$ when $Y(t)$ is clutterlike. Rather than allow $Y_0(t)$ to take on an *a priori* constant or functional value, it is necessary to establish the threshold by some means that adapts $Y_0(t)$ to the prevailing background conditions.

Proper operation of the processor requires that $Y(t) < Y_0(t)$ when there is no target in the sensor's field of view. A threshold-crossing event is defined as taking place at any time t_{TC}

such that $Y(t_{TC}) = Y_0(t_{TC})$. All threshold crossing detectors are presumed to be sensitive only to positive-slope crossings, for which*

$$\dot{Y}(t_{TC}) > \dot{Y}_0(t_{TC}). \quad (1)$$

Since the current $Y(t)$ is a random process due to time-of-arrival fluctuations of the light quanta incident on the detector,

- threshold crossings are random events,
- the threshold-crossing times t_{TC} are random variables, and
- the number of threshold crossings (J) that occur during a specified time interval is an integer random variable.

We define the average value of J as the mean crossing count m_J :

$$m_J = E\{J\}, \quad (2)$$

where the statistical expectation operator $E\{\cdot\}$ denotes an average value over the photon fluctuation statistics of the incident light [1].

We now introduce a threshold-crossing rate \dot{m}_J to help explain the relationship between m_J and the conventional search-set performance measures P_D and FAR [1]. By definition

$$m_J \equiv \int_{I_0} \dot{m}_J(t) dt, \quad (3)$$

where I_0 is an appropriately chosen time interval.

It is generally found that the principal contributions to the crossing-count integral in Eq. (3) accrue in the neighborhood of a discrete set of times which in turn can each be associated with a structural feature in the scene. As theIRST sensor scans across a target (or a background feature that simulates a target), the crossing rate $\dot{m}_J(t)$ becomes a sharply peaked, pulselike waveform.

We now define the time interval I_i as the entire period of time during which the sensor is scanned across a single structural feature in the scene (such as a local maximum in the radiance distribution). By presumption, I_i is a subinterval of the total scan interval I_0 in Eq. (3). It can be shown that the increment in m_J associated with the interval I_i , that is,

$$\Delta m_J(I_i) \equiv \int_{I_i} \dot{m}_J(t) dt, \quad (4)$$

is generally a number between 0 and 1:

$$0 < \Delta m_J(I_i) < 1. \quad (5)$$

We show in Part I [1] that $\Delta m_J(I_i)$ may be interpreted as the probability of a threshold crossing sometime during the interval I_i , that is, as the probability of a target declaration during the time interval I_i .

*By convention a dotted variable denotes the time derivative of the corresponding undotted variable.

If the structural feature scanned during the interval I_i is known *a priori* to be a target, we interpret the probability of target declaration as a probability of target detection:

$$P_D = \Delta m_J(I_i). \quad (6)$$

Conversely, if the IRST sensor is known *a priori* to be scanning a region in space that does not contain a target during I_i , we interpret the quantity $\Delta m_J(I_i)$ as the probability of a false alarm during the interval I_i :

$$P_{FA}(I_i) = \Delta m_J(I_i). \quad (7)$$

Dividing the total scan interval I_0 into a succession of disjoint subintervals I_i , each of which brackets an identifiable structural feature in the scene, we can write the overall false-alarm rate as the expected number of false alarms during I_0 divided by the duration of I_0 :

$$\text{FAR} = \frac{1}{T(I_0)} \sum_i P_{FA}(I_i). \quad (8a)$$

Thus, from Eq. (7),

$$\text{FAR} = \frac{1}{T(I_0)} \sum_i \Delta m_J(I_i) \quad (\text{false alarms per second}), \quad (8b)$$

where $T(I_0)$ is the duration of time interval I_0 (seconds) and $P_{FA}(I_i) = \Delta m_J(I_i)$ is the probability of a false alarm during time interval I_i .

In summary, target detections and false alarms are both manifested by the signal processor as threshold crossings. Consequently we can express the search-set performance measures P_D and FAR in terms of a threshold-crossing-rate function $\dot{m}_J(t)$.

Following the next subsection we will formulate the crossing rate \dot{m}_J in terms of appropriate characterizations of the IRST sensor and the background scene under observation. We will develop the formulation for the threshold-crossing rate \dot{m}_J in two steps [1]:

- First, we will express the quantities $m_Y(t)$ and σ_Y^2 as functions of the scene radiance distribution and various optical and electrical attributes of the IRST device. We will define the quantities $m_Y(t)$ and $\sigma_Y^2(t)$ as the ensemble mean value and variance of the filtered current $Y(t)$ (Fig. 1). Analogous expressions for the mean and variance of $\dot{Y}(t)$, $Y_0(t)$, and $\dot{Y}_0(t)$ are also required, and we will present them. All such mean values and variances, individually and collectively, are referred to as the current statistics of the IRST sensor.

- We will express $\dot{m}_J(t)$ in terms of the current statistics (as a function of m_Y, σ_Y , etc.).

The expression for the threshold-crossing statistic \dot{m}_J in terms of the statistics of $Y(t)$ and $Y_0(t)$ is devoid of physical content: it applies equally well to any nonstationary Gaussian process. We will introduce all of the physical parameters - the optical and electrical characteristics of the IRST device and the radiance of the background scene - through the formulation for the current statistics.

Current Statistics

The primary current statistic of interest is the average value $m_X(t)$ of the detected photocurrent $X(t)$ (Fig. 1):

$$m_X(t) = E\{X(t)\}. \quad (9)$$

As in Appendix A, $m_X(t)$ can be written as a function of the scene radiance distribution and a number of important IRST sensor parameters.

The detected current $X(t)$ and filtered current $Y(t)$ are related by the linear system-input/output relation

$$Y(t) = \int_{-\infty}^{\infty} h(t-\tau) X(\tau) d\tau \equiv h(t) \odot X(t). \quad (10)$$

The symbol \odot is a shorthand notation for the convolution process defined by the integral expression in Eq. (10). Also, $h(t)$ in Eq. (10) is the impulse response of the postdetector filter; that is, $h(t)$ is the Fourier inverse of the filter characteristic $H(f)$ in Fig. 1:

$$H(f) = \int_{-\infty}^{\infty} h(t) \exp(-j2\pi ft) dt. \quad (11)$$

When the expected value is taken of both sides of Eq. (10), it follows directly from Eq. (9) that

$$m_Y(t) \equiv E\{Y(t)\} = h(t) \odot m_X(t). \quad (12)$$

The following relationship can also be found directly from Eq. (10):

$$m_{\dot{Y}}(t) \equiv E\{\dot{Y}(t)\} = \dot{m}_Y(t). \quad (13)$$

Expressions similar to Eq. (12) are also required for the quantities $\sigma_Y^2(t)$ and $\sigma_{\dot{Y}}^2(t)$, where by definition

$$\sigma_Y^2(t) \equiv E\{[Y(t) - m_Y(t)]^2\} \quad (14)$$

and

$$\sigma_{\dot{Y}}^2(t) \equiv E\{[\dot{Y}(t) - \dot{m}_Y(t)]^2\}. \quad (15)$$

An adaptation of Eq. (4.3.13) in Ref. 6 leads to

$$\sigma_Y^2(t) = eh^2(t) \odot m_X(t), \quad (16)$$

where e is the electronic charge and $h(t)$ and $m_X(t)$ are the same quantities as in Eq. (12). As in Appendix B of Part I [1], it follows from Eqs. (10) and (16) that

$$\sigma_{\dot{Y}}^2(t) = e[\dot{h}(t)]^2 \odot m_X(t). \quad (17)$$

For the special case of spatially uniform scenes, the analysis of Appendix A shows that m_X is time independent. It then follows from Eq. (12) that

$$m_Y = m_X \int_{-\infty}^{\infty} h(t) dt. \quad (18)$$

However, from Eq. (11)

$$H(0) = \int_{-\infty}^{\infty} h(t) dt. \quad (19)$$

Thus, from Eqs. (18) and (19)

$$m_Y = H(0)m_X \quad (20)$$

for uniform backgrounds. For bandpass transfer functions, $H(0) = 0$. It follows from Eq. (20) that $Y(t)$ is a zero-mean process for the special case of uniform backgrounds and bandpass postdetector filters.

Similarly it can be shown from the Parseval relation for Fourier transforms

$$\int_{-\infty}^{\infty} h^2(t) dt = \int_{-\infty}^{\infty} |H(f)|^2 df \quad (21)$$

that Eqs. (16) and (17) simplify as follows in the uniform background limit:

$$\sigma_Y^2 = em_X \int_{-\infty}^{\infty} |H(f)|^2 df \quad (22)$$

and

$$\sigma_{\dot{Y}}^2 = em_X \int_{-\infty}^{\infty} (2\pi f)^2 |H(f)|^2 df. \quad (23)$$

Assuming that the transfer characteristic $H(f)$ has been normalized to a peak value of unity, that is,

$$\max_f H(f) = 1, \quad (24)$$

we define the conventional noise bandwidth of $H(f)$ as

$$\Delta f \equiv \int_0^{\infty} |H(f)|^2 df. \quad (25)$$

It follows from Eqs. (22) and (25) that

$$\sigma_{\dot{Y}}^2 = 2em_X \Delta f, \quad (26)$$

which is the usual Poisson shot-noise variance formula (given in, for example, Ref. 7). By inference Eq. (16) is a generalization of the usual shot-noise variance expression to nonstationary shot-noise processes.

The motivation for the results presented in this subsection is provided in the following subsection, in which we express the threshold-crossing rate $\dot{m}_j(t)$ as a function of the current statistics. (It should be recalled from the Concepts and Definitions subsection that the usual search-set performance measures P_D and FAR may then be calculated in terms of the crossing rate \dot{m}_j .)

In summary, the current statistics m_Y , $m_{\dot{Y}}$, σ_Y , and $\sigma_{\dot{Y}}$ may all be written as relatively simple functions of the postdetector filter impulse response $h(t)$ and the average value $m_X(t)$ of the unfiltered current $X(t)$ (Fig. 1):

$$m_Y(t) = h(t) \oplus m_X(t), \quad (27)$$

$$m_{\dot{Y}}(t) = \dot{m}_Y(t), \quad (28)$$

$$\sigma_Y^2(t) = eh^2(t) \oplus m_X(t), \quad (29)$$

and

$$\sigma_{\dot{Y}}^2(t) = e[\dot{h}(t)]^2 \oplus m_X(t). \quad (30)$$

Expressions for the threshold-current statistics can be written directly by analogy to Eqs. (27) through (30) for the threshold approach depicted in Fig. 2:

$$m_{Y_0}(t) = K h_0(t - T_d) \otimes m_X(t), \quad (31)$$

$$m_{\dot{Y}_0}(t) = \dot{m}_{Y_0}(t), \quad (32)$$

$$\sigma_{Y_0}^2(t) = eK h_0^2(t - T_d) \otimes m_X(t), \quad (33)$$

and

$$\sigma_{\dot{Y}_0}^2(t) = eK [\dot{h}_0(t - T_d)]^2 \otimes m_X(t), \quad (34)$$

where K and T_d are the gain and time delay respectively in the threshold circuitry and $h_0(t)$ is the Fourier inverse of the threshold filter characteristic $H_0(f)$ (Fig. 2).

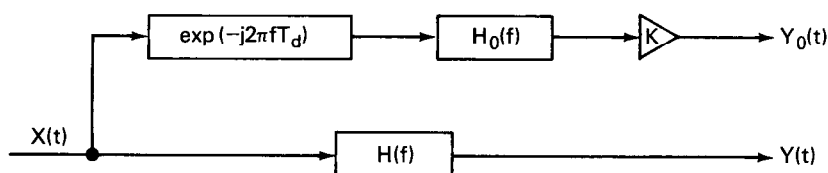


Fig. 2 — A simple adaptive-threshold scheme. The transfer function $\exp(-j2\pi f T_d)$ introduces a delay of T_d seconds, ensuring decorrelation of the random processes $Y(t)$ and $Y_0(t)$. Figure 1 shows the significance of the random signals $X(t)$, $Y(t)$, and $Y_0(t)$.

The mean unfiltered current $m_X(t)$ that figures so prominently in Eqs. (27) through (34) is expressed in Appendix A as a function of the scene radiance distribution and a number of important IRST sensor parameters.

Threshold-Crossing Rates

We will now briefly outline the method developed in Part I [1] for calculating the average number of times m_J that the random current $Y(t)$ crosses the random threshold $Y_0(t)$ during a specified time interval (Figs. 1 and 2). The relationship between the mean crossing count m_J and the usual search-set parameters P_D and FAR was briefly discussed in the Concepts and Definitions subsection of this report and discussed in greater depth in Part I [1].

We first express the crossing count as the time integral of a threshold crossing rate $\dot{m}_J(t)$ (Eq. 3). We then write the crossing rate \dot{m}_J as a function of the current statistics as*

$$\dot{m}_J(t) = \dot{m}_{J_0}(t) \exp[-u^2(t)/2], \quad (35)$$

where by definition

$$\dot{m}_{J_0}(t) \equiv (2\pi)^{-1} (\sigma_{\dot{Y}_0} / \sigma_{Y_0}). \quad (36)$$

*Equation (35) for \dot{m}_J is not strictly valid in the neighborhood of "mean-crossing times" (to be defined by Eq. (42)). A more general formulation for \dot{m}_J valid everywhere is derived in Part I [1]. However, as we will note following Eq. (42), the more general expression for \dot{m}_J is not usually required, since it integrates to unity in the neighborhood of a mean crossing [1,2].

Also,

$$\sigma_{\dot{Y}Y_0}^2 \equiv \sigma_{\dot{Y}}^2 + \sigma_{Y_0}^2, \quad (37)$$

$$\sigma_{\dot{Y}\dot{Y}_0}^2 \equiv \sigma_{\dot{Y}}^2 + \sigma_{\dot{Y}_0}^2, \quad (38)$$

and

$$u(t) \equiv (m_{Y_0} - m_Y)/\sigma_{Y_0}. \quad (39)$$

As indicated by Eqs. (4), (6), and (8), evaluation of the important search-set parameters P_D and FAR requires the time integration of Eq. (35) to obtain the mean crossing count m_J over prescribed intervals of time:

$$m_J = \int_{I_1} \dot{m}_J(t) dt, \quad (40)$$

where I_1 is the time interval of interest.

When $m_X(t)$ is slowly varying compared to $h(t)$, it can be shown that $\dot{m}_{J_0}(t)$ is practically constant with time (as will be expressed by Eq. (48)). In this case, it follows from Eqs. (35) and (40) that

$$m_J \cong \dot{m}_{J_0} \int_{I_1} \exp[-u^2(t)/2] dt. \quad (41)$$

As we will now discuss, the integration in Eq. (41) is often quite simple to perform.

Mean-Crossing Times and Times of Closest Approach

Experience with the numerical evaluation of Eq. (41) has shown that the principal contributions to the integral accrue in the neighborhood of a discrete set of times. Moreover, it has been shown that these important discrete times are of two types: "mean-crossing times" and "closest-approach times" [1,2].

As illustrated in Fig. 3a, the mean-crossing times t_{mc} are those times that simultaneously satisfy the two conditions

$$m_Y(t_{mc}) = m_{Y_0}(t_{mc}) \quad (42)$$

and

$$\dot{m}_Y(t_{mc}) > \dot{m}_{Y_0}(t_{mc}). \quad (43)$$

For each solution of Eq. (42) that satisfies constraint (43), that is, each time the mean current $m_Y(t)$ crosses the mean threshold $m_{Y_0}(t)$ with positive slope, the expected number of crossings m_J is incremented by unity. Whenever mean crossings exist during the interval I_1 , it is generally not necessary to perform the integration in Eq. (40); in this case the expected number of threshold crossings m_J is well approximated by the number of mean-crossing times t_{mc} during the interval I_1 . Thus, the expression for \dot{m}_J is generally not needed to evaluate the contributions to m_J that occur in the neighborhood of mean crossings, since each mean crossing gives

rise to a threshold crossing [1].* Clearly it is desirable that no mean crossings occur except when there is a point target in the scene; this may be taken as the first principle of search-set design for operation against structured backgrounds.

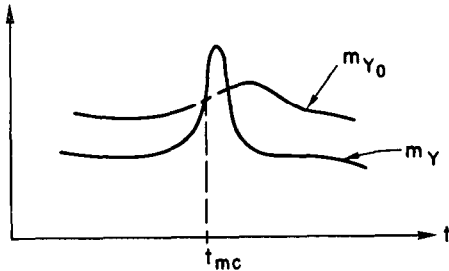


Fig. 3a — A "mean-crossing time" denoted t_{mc} . A mean crossing occurs when the mean video signal m_Y crosses the mean threshold signal m_{Y_0} with positive slope. Asymptotic evaluation of the crossing-rate integral, Eq. (40), shows that the probability of a threshold crossing approaches unity in the neighborhood of a mean-crossing time t_{mc} [1].

If $m_Y(t)$ lies below $m_{Y_0}(t)$ on the time interval I_1 , that is, if there are no mean crossings during I_1 , the crossing-count integral, Eq. (40), is generally dominated by contributions accruing in the neighborhood of "times of closest approach." As illustrated in Fig. 3b, closest-approach times are those times that satisfy the equation

$$m_{\dot{Y}_0}(t_{ca}) = m_{\dot{Y}}(t_{ca}). \quad (44)$$

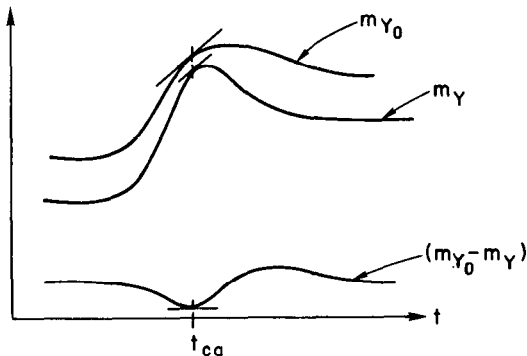


Fig. 3b — A "closest-approach time," denoted t_{ca} . The threshold-crossing rate \dot{m}_j typically increases many orders of magnitude in the immediate neighborhood of a closest-approach time.

Fixed-Threshold Processors

For fixed-threshold (FT) processors

$$\sigma_{Y_0} = \sigma_{\dot{Y}_0} = 0 \quad (45a)$$

and

$$m_{Y_0} = y_0. \quad (45b)$$

*Although a threshold crossing is assured in the near neighborhood of a mean crossing, the threshold-crossing time t_{TC} is not equal to the mean-crossing time t_{mc} , since t_{TC} is a random variable (as stated following Eq. (1)), while t_{mc} is deterministic.

It follows from Eqs. (35) through (39) and (45) that

$$\dot{m}_J(t) = (2\pi)^{-1} (\sigma_Y/\sigma_Y) \exp[-u^2(t)/2], \quad (46)$$

where

$$u(t) = (y_0 - m_Y)/\sigma_Y. \quad (47)$$

The current statistics m_Y , σ_Y , and σ_Y in Eqs. (46) and (47) are obtained from Eqs. (27) through (30), and y_0 in Eq. (47) is a fixed threshold value.

When $m_X(t)$ is slowly varying compared to $h(t)$, it follows from Eqs. (23) and (26) that

$$\dot{m}_{J_0} = (2\pi)^{-1} (\sigma_Y/\sigma_Y) \cong \left[(\Delta f)^{-1} \int_0^\infty f^2 |H(f)|^2 df \right]^{1/2} \equiv (\Delta f)_{rms}. \quad (48)$$

Equations (41) and (48), taken together, provide a relatively simple formalism for calculating the expected crossing count of a fixed-threshold receiver operating against a slowly varying background scene.

In the limit of time-invariant m_X (perfectly uniform backgrounds) Eq. (41) simplifies still further to

$$m_J = (\Delta f)_{rms} \exp(-K^2/2) \cdot T(I_1), \quad (49)$$

where $T(I_1)$ is the duration of I_1 , $(\Delta f)_{rms}$ is once again given by Eq. (48), and the fixed threshold y_0 has presumably been adjusted such that

$$u = (y_0 - m_Y)/\sigma_Y = K. \quad (50)$$

Equation (49) is originally due to Rice [8] and has often been applied to the calculation of false-alarm rates for infrared search-set operation against uniform scenes [9,10].

Initial Assessment of Adaptive Vs Fixed-Threshold Processors

Some of the advantages and disadvantages of adaptive-threshold (AT) processing as compared with fixed threshold (FT) processing may be evaluated by comparing Eqs. (39) and (47), appropriate for AT and FT receivers respectively.

It follows from Eq. (47) that an FT processor suffers a false alarm whenever the peak target amplitude is less than the peak clutter amplitude. This situation is depicted in Fig. 4a. Thus target-to-clutter ratios less than unity cause the FT processor performance to be "background-structure limited" (BSL). In this case each false alarm can be associated with a structural feature in the background. The effect of quantum noise (as reflected in the magnitude of σ_Y , for example) is then totally overshadowed by background-structure effects.

Inspection of Eq. (39) and Fig. 4b shows that an adaptive-threshold (AT) processor need not suffer background-induced mean crossings. If the filter $H_0(f)$ (Fig. 2) can be chosen such that $m_{Y_0}(t)$ tracks the background-induced variations in $m_Y(t)$, the background-induced mean crossings can be eliminated. Although false alarms may still occur as random events due to quantum noise, the probability is generally small that any given structural feature in the scene will cause a false alarm.

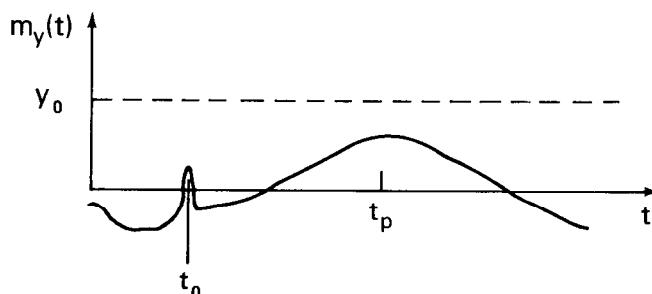


Fig. 4a — A critical shortcoming of fixed-threshold processing. The slowly varying maximum centered at t_p has its origin in the nonuniform background scene. The narrower peak at t_0 is due to a target. The likelihood of a false alarm grows rapidly as the threshold level y_0 is reduced. There is no way for the constant-threshold processor to detect the target peak at t_0 without also incurring a false alarm arising from the clutter peak centered at t_p . A plot of the threshold-crossing rate $\dot{m}_Y(t)$ corresponding to this figure would show that the probability of a threshold crossing, and hence a false alarm, is far greater at time t_p than at any other time, since t_p is a time of closest approach.

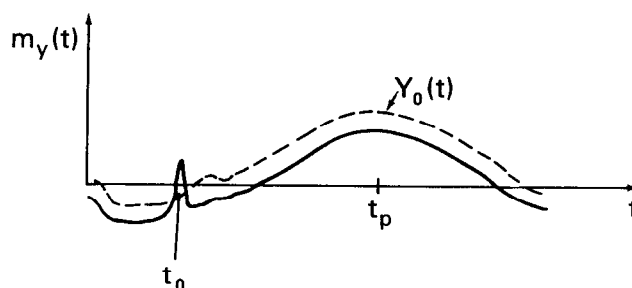


Fig. 4b — An important advantage of adaptive threshold processing. The mean current $m_Y(t)$ is the same as for Fig. 4a. The adaptive threshold $Y_0(t)$ accurately tracks the slowly varying background signal but not the more rapidly varying target signal. Thus, target detection is assured, and the probability of a false alarm is kept acceptably small. As contrasted with the situation of Fig. 4a, the probability of a false alarm is now no greater in the neighborhood of time t_p than at any other time.

An IRST sensor operating in this regime (such as in Fig. 4b) is said to be "quantum-noise limited" (QNL) in its performance. In this context QNL operation is clearly preferable to BSL (background-structure-limited) operation.

Uniform Scenes of Known Brightness

The adaptive-threshold-performance advantage just described is realized only when the background scene is nonuniform. The performance of an adaptive-threshold processor is inferior to the performance of a properly designed FT processor when the background scene is uniform and of known brightness. In this case the adaptive-threshold false-alarm rate (FAR_{AT}) is greater (worse) than the fixed-threshold false-alarm rate (FAR_{FT}):

$$\text{FAR}_{\text{AT}} > \text{FAR}_{\text{FT}}. \quad (51)$$

For the false-alarm-rate comparison expressed by Eq. (51) to be meaningful, the adaptive-threshold gain K in Fig. 2 has been adjusted to achieve equal target-detection sensitivities for the two processors being compared.

We now define uniform-background false-alarm-penalty (FAP):

$$\text{FAP} \equiv 10 \log_{10} (\text{FAR}_{\text{AT}}/\text{FAR}_{\text{FT}}) \text{ dB}. \quad (52)$$

Uniform-Background False-Alarm-Penalty

The uniform-background false-alarm penalty is a measure of the performance disadvantage that accrues when an AT processor is used against a uniform-background scene of known brightness. As shown in Part I [1], the false-alarm penalty of the processor structure in Fig. 2 may be written as

$$\text{FAP} = 2.17 \left[\frac{\alpha}{1 + \alpha} \right] \left[\frac{m_{Y_0} - m_Y}{\sigma_Y} \right]^2 + 5 \log_{10} [1 - \alpha(1 - \alpha)] \text{ dB}. \quad (53)$$

where by definition

$$\alpha \equiv \Delta f_0 / \Delta f \quad (54)$$

and where Δf and Δf_0 are defined as the noise-equivalent bandwidths of $H(f)$ and $H_0(f)$, respectively (Eq. (25) and Fig. 2).

As an example, we assume that the threshold constant K in Fig. 2 is adjusted until "the threshold is five sigmas above the mean," that is,

$$\left[\frac{m_{Y_0} - m_Y}{\sigma_Y} \right] = 5, \quad (55)$$

when the search set is observing a uniform scene of known brightness. Furthermore we assume that the noise bandwidth of the target filter $H(f)$ in Fig. 2 is twice as large as the noise bandwidth of the threshold filter $H_0(f)$:

$$\alpha = \frac{\Delta f_0}{\Delta f} = \frac{1}{2}. \quad (56)$$

It follows from Eqs. (53) through (56) that the false-alarm penalty is

$$\text{FAP} = 17.46 \text{ dB}, \quad (57)$$

corresponding to a value of FAR_{AT} (adaptive-threshold false-alarm rate) about 56 times worse than FAR_{FT} (fixed-threshold false-alarm rate). Clearly this is a severe degradation in performance.

Time Delay and Integration

Fortunately the disadvantage of AT processing can be more than recovered by means of time delay and integration (TDI). The effect of TDI is simply to multiply the mean current $m_X(t)$ by the number N of series TDI detectors. It follows from Eqs. (27) and (29) that TDI multiplies m_Y and σ_Y by the factors N and $N^{1/2}$ respectively. It can be shown that

$$FAP_{TDI} = \left[\frac{1 + \alpha - N}{\alpha} \right] \left[2.17 \left(\frac{\alpha}{1 + \alpha} \right) \left(\frac{m_{Y_0} - m_Y}{\sigma_Y} \right)^2 \right] + 5 \log_{10}[1 - \alpha(1 - \alpha)] \quad (58)$$

for the AT processor depicted in Fig. 2, employing N series TDI detectors. It follows from Eqs. (55), (56), and (58) that

$$FAP_{TDI} = [(3 - 2N) (18.08) - 0.62] \text{ dB} \quad (59)$$

for the example given. Thus the uniform-background false-alarm penalty suffered by the AT processor of Fig. 2 is more than compensated by the use of just $N = 2$ TDI detectors. Apparently the false-alarm rate can be made arbitrarily small by increasing the number of TDI detectors. Alternatively the false-alarm rate can be held constant with increasing N by making the threshold gain K (Fig. 2) inversely proportional to $N^{1/2}$. The TDI performance advantage is then realized as a target-detection sensitivity enormously increased over that of the $N = 1$ single-detector IRST sensor. IRST performance against uniform scenes improves monotonically as the number of TDI elements is increased.

Again, the false-alarm penalty is meaningful only as a characterization of AT processor performance against the most benign type of background—a uniform background of known brightness.* However, the motivation for employing AT processing lies in the unfortunate reality that natural-background scenes are often highly structured.

In following sections of this report we will characterize a number of candidate processing schemes with respect to their performance against a succession of more complex scenes. We discuss the rationale underlying the design of these candidate processors in the following subsection.

Ideal (CFAR) Adaptive-Threshold Receivers

The candidate processor designs described in this report each consist of two parts: one part for estimating the mean video signal m_Y , and a second part for estimating the rms quantum noise σ_Y . The signal processor establishes the adaptive threshold $Y_0(t)$ as shown in Fig. 5:

$$Y_0(t) = \hat{m}_Y(t) + K \hat{\sigma}_Y(t), \quad (60)$$

*The relevance of scene radiance m_L to search-set performance against uniform scenes follows directly from Eqs. (26) and (A5). The noise variance σ_Y^2 increases linearly with scene radiance m_L . Thus operation against bright uniform scenes occasions decreased target detection sensitivity and/or increased false-alarm rate as compared with operation against uniform scenes of lesser brightness.

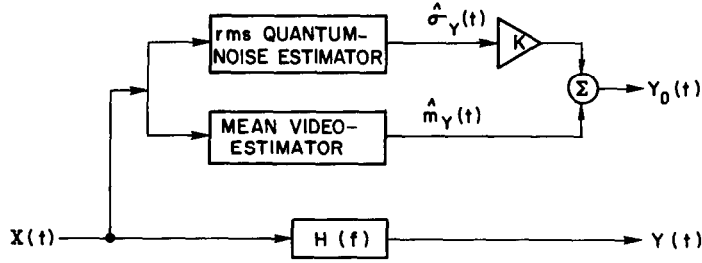


Fig. 5 — Generic structure of the signal processors considered in this report. The expected value and rms value of the video signal $Y(t)$ are denoted as $m_Y(t)$ and $\sigma_Y(t)$ respectively. The signals $\hat{m}_Y(t)$ and $\hat{\sigma}_Y(t)$ are estimates for $m_Y(t)$ and $\sigma_Y(t)$. The adaptive-threshold constant K is the gain of an ideal amplifier. As shown in Fig. 1, a target's presence is declared (rightly or wrongly) whenever the video signal $Y(t)$ exceeds the threshold signal $Y_0(t)$.

where \hat{m}_Y and $\hat{\sigma}_Y$ are estimates for m_Y and σ_Y respectively. The adaptive threshold constant K in Eq. (60) is a design parameter. The estimates \hat{m}_Y and $\hat{\sigma}_Y$ and the threshold Y_0 are all stochastic processes. With the expected values of \hat{m}_Y and $\hat{\sigma}_Y$ denoted as $m_{\hat{m}_Y}$ and $m_{\hat{\sigma}_Y}$ respectively, it follows from Eqs. (39) and (60) that

$$u(t) = K(m_{\hat{\sigma}_Y}/\sigma_{YY_0}) + (m_{\hat{m}_Y} - m_Y)/\sigma_{YY_0}. \quad (61)$$

Equation (61) can be written as

$$u(t) = K(1 + \epsilon_{\hat{\sigma}_Y}) + \chi \epsilon_{\hat{m}_Y}, \quad (62)$$

where the normalized mean estimation errors $\epsilon_{\hat{m}_Y}$ and $\epsilon_{\hat{\sigma}_Y}$ are defined as

$$\epsilon_{\hat{m}_Y} \equiv (m_{\hat{m}_Y} - m_Y)/m_Y \quad (63)$$

and

$$\epsilon_{\hat{\sigma}_Y} \equiv (m_{\hat{\sigma}_Y} - \sigma_{YY_0})/\sigma_{YY_0}. \quad (64)$$

Also, as will be expressed by Eq. (C6),

$$\chi \equiv (m_Y/\sigma_{YY_0}) = O(10^3), \quad (65)$$

and

$$K = O(10). \quad (66)$$

When no target is in the sensor's field of view, "ideal" receiver performance is expressed in terms of the estimation errors as

$$|\epsilon_{\hat{m}_Y}| \ll \chi^{-1} = O(10^{-3}) \quad (67)$$

and

$$|\epsilon_{\hat{\sigma}_Y}| \ll K^{-1} = O(10^{-1}). \quad (68)$$

From Eqs. (62), (67), and (68)

$$u(t) \cong K. \quad (69)$$

Thus Eqs. (67) and (68) assure that $u(t)$ is rendered time invariant by the AT processor when no target is in the sensor's field of view.

From Eqs. (41) and (69),

$$m_J = \text{FAR} \cdot T(I_1) = \dot{m}_{J_0} \exp(-K^2/2) \cdot T(I_1). \quad (70)$$

Equation (70) is identical to the crossing-count expression for uniform scenes, Eq. (49).

The kind of processor just described is called a constant-false-alarm-rate (CFAR) processor, since the threshold-crossing rate is now independent of time; that is, a crossing is no more likely to occur during scanning of a region of nonuniform background than during scanning of a region of uniform background. With reference to Fig. 4b for example, the crossing rate is now no greater at t_p than at any other time.

Unfortunately the CFAR processor is generally a nonrealizable ideal. Depending on the structural features present in the background radiance distribution, large estimation errors $\epsilon_{\dot{m}_Y}$ and ϵ_{σ_Y} may be unavoidable, giving rise to appreciable time dependence in Eq. (62) for $u(t)$. We will show numerical examples that illustrate this point in Figs. 11b, 12, 14, and 15.

When a target is in the sensor's field of view, "ideal" receiver performance is obtained when the time interval I_i bracketing the target scan contains a mean-crossing time t_{mc} , for which (Eqs. (42) and (39))

$$u(t_{mc}) = 0. \quad (71)$$

As we discussed following Eq. (42), a mean crossing assures that [1]

$$P_D = m_J \cong 1, \quad (72)$$

as desired.

Mean-Video Estimators

Comparison of Eqs. (67) and (68) shows that the requirement on $\epsilon_{\dot{m}_Y}$ for ideal receiver performance is two orders of magnitude more severe than the requirement on ϵ_{σ_Y} . In this sense the mean-video estimator may be deemed a more critical component than the rms quantum-noise estimator.

In the following sections we will concentrate our discussion of mean-video estimators on three types of linear filters (Table 1), evaluating their performance against a succession of increasingly complex model backgrounds:

- uniform scenes of known radiance,
- uniform scenes of unknown radiance,
- slowly varying nonuniform scenes, and
- scenes containing objects of arbitrary contrast and size (such as a target).

Table 1 — Candidate mean-video estimators. All of the adaptive-threshold signal processors we consider in this report have the generic form indicated in Fig. 5, incorporating a filter for estimating the expected value of the video signal $Y(t)$. We consider the use of three types of linear filters as candidate mean-video estimators in order to illustrate our approach to processor design and evaluation.

Signal Processor	Mean-Video Estimate $\hat{m}_Y(t)$
Fig. 6	0
Fig. 10	$Y(t - T_d)$
Fig. 13	$1/2 [Y(t - T_d) + Y(t + T_d)]$

Greatly improved mean-video estimators can no doubt be developed by incorporating actual measured background scenes into the processor-design-and-evaluation procedure and by expanding the scope of candidate processor designs to include nonlinear algorithms as well as linear ones.

UNIFORM SCENES OF UNKNOWN BRIGHTNESS

In this section we will illustrate the potential advantage of adaptive-threshold (AT) processing over fixed-threshold (FT) processing by analyzing IRST performance against the simplest possible type of incompletely specified scene: the uniform scene of unknown brightness.

We will first show that the unknown brightness level can badly degrade the performance of an FT system. We will then analyze the AT processor structure of Fig. 6 and show it can maintain the same false-alarm rate (FAR) against all uniform scenes regardless of brightness. In other words the Fig. 6 processor is said to operate in the constant-false-alarm-rate (CFAR) regime against the class of uniform backgrounds of unknown brightness.

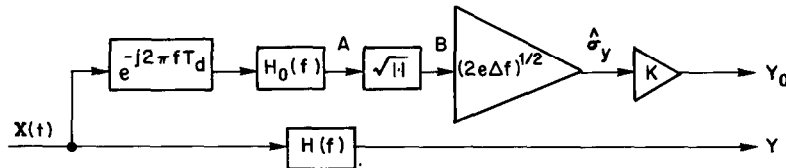


Fig. 6 — Candidate processor structure that achieves constant-false-alarm-rate (CFAR) performance against all spatially uniform scenes regardless of brightness. The transfer functions $H(f)$ and $H_0(f)$ are related by Eq. (B1). Realization of $H_0(f)$ requires either true dc response or dc restoration. Comparing this figure with Fig. 5 shows that the mean video has been estimated as having a zero value. A unique feature of this processor is that the expected value of $\hat{\sigma}_Y$ is equal to the rms value of $Y(t)$ (as shown in Appendix B).

Fixed-Threshold Processors

We analyze the false-alarm-rate performance of an FT processor against a uniform scene by use of Eqs. (49), (50), and (20) with the assumption that $H(0) = 0$, resulting in

$$\text{FAR} = (\Delta f)_{rms} \exp \left[-\frac{1}{2} (y_0/\sigma_Y)^2 \right]. \quad (73)$$

It follows from Eqs. (26) and (A5) that the current variance σ_Y^2 [A^2] in Eq. (73) is directly proportional to the scene radiance m_L [$W \cdot cm^{-2} \cdot sr^{-1}$]:

$$\sigma_Y^2 = C m_L, \quad (74a)$$

where

$$C \equiv (2e \Delta f K_o R_f A_{det}). \quad (74b)$$

We define the quantities K_o , R_f , and A_{det} in Appendix A.

For illustration we assume that an acceptably low false-alarm rate is achieved by choosing the fixed threshold y_0 in Eq. (73) as follows:

$$y_0 = 8 \sigma_{YC} = 8 (C m_{LC})^{1/2}, \quad (75)$$

where m_{LC} is the radiance of the scene chosen to initially calibrate the IRST and σ_{YC} is the corresponding value of σ_Y obtained from Eq. (74). It follows from Eqs. (73) through (75) that the false-alarm rate is given by

$$\text{FAR} = \text{FAR}_c \exp [32(m_L - m_{LC})/m_L], \quad (76)$$

where FAR_c is the calibration value of FAR:

$$\text{FAR}_c \equiv (\Delta f)_{rms} \exp(-32). \quad (77)$$

It follows from Eq. (76) that a 20% increase in the scene radiance above the calibration value,

$$m_L = 1.2 m_{LC}, \quad (78)$$

causes a 200-fold degradation (increase) in the false-alarm rate.

This simple example clearly demonstrates that large-scale uncertainties in the false-alarm-rate performance of fixed-threshold processors are induced by relatively small uncertainties in scene brightness.

Adaptive-Threshold Processors

In this subsection we analyze the false-alarm-rate (FAR) performance of the adaptive-threshold processors depicted in Figs. 2 and 6 against uniform scenes of unknown brightness.

As discussed in Part I [1], Eqs. (37) and (38) simplify as follows for uniform backgrounds for the Fig. 2 processing structure:

$$\sigma_{\dot{Y}_0}^2 = \sigma_{\dot{Y}}^2 (1 + \alpha) \quad (79)$$

and

$$\sigma_{\dot{Y}_0}^2 \cong \sigma_{\dot{Y}}^2 (1 + \alpha^3), \quad (80)$$

where α is defined by Eq. (54) as the ratio of the noise bandwidths of $H_0(f)$ and $H(f)$. From Eqs. (35), (36), (39), (48), (79), and (80)

$$\text{FAR} = (\Delta f)_{\text{rms}} \left[\frac{1 + \alpha^3}{1 + \alpha} \right]^{1/2} \exp \left[\frac{-1}{2(1 + \alpha)} \left(\frac{m_{Y_0} - m_Y}{\sigma_Y} \right)^2 \right]. \quad (81)$$

If $H(f)$ is a bandpass characteristic, so that $H(0) = 0$, it follows from Eq. (20) that

$$m_Y = H(0) m_X = 0. \quad (82)$$

We assume that $H_0(f)$ is a low-pass characteristic, normalized analogous to Eq. (24):

$$\max_f H_0(f) = H_0(0) = 1. \quad (83)$$

From Eq. (83) and by analogy to Eq. (20)

$$m_{Y_0} = K H_0(0) m_X = K m_X, \quad (84)$$

where K is the threshold gain, as shown in Fig. 2.

From Eqs. (82) and (84)

$$\left(\frac{m_{Y_0} - m_Y}{\sigma_Y} \right)^2 = \left(\frac{m_{Y_0}}{\sigma_Y} \right)^2 = K^2 (m_X / \sigma_Y)^2. \quad (85)$$

From Eqs. (85), (26), and (A5)

$$\left(\frac{m_{Y_0} - m_Y}{\sigma_Y} \right)^2 = K^2 \left(\frac{m_X^2}{2e \Delta f m_X} \right) \propto m_L. \quad (86)$$

It follows from Eq. (86) that the argument of the exponential in Eq. (81) is linearly proportional to the scene radiance m_L . Thus the false-alarm-rate performance of the AT processor depicted in Fig. 2, like the FT processor analyzed in the previous subsection, strongly depends on the scene brightness. This is due to the incomplete cancellation of the m_X factors in the numerator and denominator of Eq. (86): $m_{Y_0}^2$ is proportional to m_X^2 , but σ_Y^2 is proportional to m_X . We remedy this situation in Fig. 6, by including a square-root device in the threshold circuitry.

Figure 6 shows that

$$Y_0(t) = K \hat{\sigma}_Y(t). \quad (87)$$

From Eqs. (60) and (87)

$$\hat{m}_Y(t) = 0 \quad (88)$$

for the Fig. 6 processor. It follows from Eqs. (61), (82), and (88) that

$$u(t) = K (m_{\hat{\sigma}_Y} / \sigma_{Y_0}). \quad (89)$$

Importantly it is shown in Appendix B that $\hat{\sigma}_Y$ as determined by the Fig. 6 processor is an unbiased estimate for σ_Y :

$$m_{\hat{\sigma}_Y} = \sigma_Y. \quad (90)$$

From Eqs. (37) and (87)

$$\sigma_{Y_0}^2 = \sigma_Y^2 [1 + K^2 (\sigma_{\hat{\sigma}_Y} / \sigma_Y)^2]. \quad (91)$$

From Eqs. (66), (90), (91), and (B6)

$$(m_{\hat{\sigma}_Y} / \sigma_{Y_0}) - 1 = O(10^{-4}) \quad (92)$$

for the Fig. 6 processor. From Eqs. (89) and (92)

$$u(t) \cong K. \quad (93)$$

From Eqs. (41) and (93)

$$\text{FAR} = (\Delta f)_{rms} \exp(-K^2/2) \quad (94)$$

for the structure shown in Fig. 6, where $(\Delta f)_{rms}$ is given by Eq. (48) and K is the adaptive-threshold gain (Fig. 6). Thus the false-alarm rate of the AT processor depicted in Fig. 6 is independent of the brightness level of the presumably spatially uniform scene.

Our discussion has so far ignored a potentially important complication: Eq. (35) is derived in Part I [1] subject to the requirement that $Y(t)$ and $Y_0(t)$ are both Gaussian random processes. However, although $Y(t)$ and $A(t)$ in Fig. 6 are each Gaussian, the square-root device ensures that $Y_0(t)$ is not Gaussian. Thus Eq. (35) is not strictly applicable to the structure of Fig. 6.

However, the following plausibility argument suggests that a rigorous treatment of this problem is probably unnecessary. It follows from Fig. 6 and Eqs. (C2) and (C6) that

$$\frac{\sigma_{Y_0}}{m_{Y_0}} = \frac{\sigma_B}{m_B} = \frac{1}{2} \left(\frac{\sigma_A}{m_A} \right) = O(10^{-3}).$$

However, from Fig. 6 and Eq. (B3)

$$m_{Y_0} = K m_{\hat{\sigma}_Y} = K \sigma_Y.$$

From the preceding two equations

$$\sigma_{Y_0} / \sigma_Y = O(10^{-3}). \quad (95)$$

According to Eq. (95) the rms fluctuation of $Y_0(t)$ is three orders of magnitude smaller than the rms fluctuation of $Y(t)$. Thus it appears unlikely that the statistics of $(Y - Y_0)$ are appreciably influenced by the statistics of Y_0 . Consequently it also appears unlikely that a more rigorous treatment of this problem would yield a result significantly different than Eq. (35).

Another important point that we brushed over is the requirement for a low-pass threshold filter (Eq. (83)). Bandpass characteristics (ac coupling) eliminate some practical problems, such as $1/f$ detector noise. However, the present analysis indicates that implementation of an effective AT processor for operation against uniform scenes of unknown brightness requires knowledge of the dc component of the photocurrent. We will find in succeeding sections of this report that dc coupling (or synthetic dc restoration [11,12]) is also required by IRST AT processors designed for operation against structured backgrounds.

STRUCTURED SCENES

We have employed two kinds of background models in the analysis thus far: uniform backgrounds of known brightness, and uniform backgrounds of unknown brightness. Moreover we have obtained a processor structure (Fig. 6) that performs extremely well against these types of backgrounds. In defining a hierarchy of increasingly realistic (and complex) background models, a reasonable next step is the consideration of slowly varying structured backgrounds.*

We will first show that the Fig. 6 processor performs poorly against the newly defined class of slowly varying backgrounds. We will establish this point by showing that the Fig. 6 processor is susceptible to background-induced mean crossings against nonpointlike background structures. The prediction of mean crossings is relatively simple, requiring only the calculation of the m_Y and m_{Y_0} current statistics. Thus we will illustrate a general principle: point-target detectors that operate poorly are easily modeled.

The deficiencies of the Fig. 6 processor suggest a modification in structure that will lead to another processor (to be depicted in Fig. 10). Our analysis of the new processor will show that it can suppress mean crossings by slowly varying backgrounds. Nonetheless we will invoke the concept of constant-false-alarm-rate (CFAR) performance to show that considerable room for improvement still remains. We will propose yet another processor structure (to be depicted in Fig. 13) toward the objective of achieving CFAR performance against slowly varying backgrounds. The Fig. 13 processor employs a variant of "linear spatial filtering" to establish the threshold process $Y_0(t)$.

Slowly Varying Scenes

Toward defining what we mean by slowly varying scenes, we rewrite Eq. (27) in the form

$$m_Y(t) = \int_{-\infty}^{\infty} h(\lambda) m_X(t - \lambda) d\lambda. \quad (96)$$

An unresolved point radiator in the field of view (such as a target) induces fluctuations in $m_X(t)$ that are as rapid as those of the filter impulse response $h(t)$.† However, we assume

*The meaning of "slowly varying" in the present context will be expressed quantitatively in the next subsection. Qualitatively it means that all objects in the field of view must be much larger than a single pixel in spatial extent. Whether or not a given scene is slowly varying thus depends on the instantaneous field of view of the sensor.

†This is assured by the usual design equation $2\Delta f T_d = 1$, where T_d is the dwell time of the sensor and Δf is the noise bandwidth of $H(f)$ [10].

here that the time variations in $m_X(t)$ are slow compared to $h(t)$, that is, that $m_X(t)$ is not targetlike. This justifies writing a three-term Taylor expansion for $m_X(t - \lambda)$,*

$$m_X(t - \lambda) \cong m_X(t) - \lambda \dot{m}_X(t) + \lambda^2 \ddot{m}_X(t)/2. \quad (97)$$

Substituting Eq. (97) into Eq. (96) yields

$$m_Y(t) \cong m_X(t) I_1 - \dot{m}_X(t) I_2 + \ddot{m}_X(t) I_3/2, \quad (98)$$

where by definition

$$I_1 \equiv \int_{-\infty}^{\infty} h(t) dt, \quad (99)$$

$$I_2 \equiv \int_{-\infty}^{\infty} t h(t) dt, \quad (100)$$

and

$$I_3 = \int_{-\infty}^{\infty} t^2 h(t) dt. \quad (101)$$

It follows from Eqs. (11) and (99) through (101) that

$$I_1 = H(0), \quad (102)$$

$$I_2 = H'(0) (-j2\pi)^{-1}, \quad (103)$$

and

$$I_3 = -H''(0) (2\pi)^{-2}, \quad (104)$$

where the primes indicate differentiation with respect to electrical frequency f . If $H(f)$ is a bandpass characteristic, then

$$H(0) = 0. \quad (105)$$

It can also be shown that

$$H'(0) = 0, \quad (106)$$

as a consequence of $h(t)$ being a real function of time. From Eqs. (98) through (106)

$$m_Y(t) \cong -(8\pi^2)^{-1} H''(0) \ddot{m}_X(t). \quad (107)$$

According to Eq. (107) the bandpass filter $H(f)$ double-differentiates a slowly varying input. The corresponding approximation to Eq. (29) for σ_Y^2 is easily shown to be

$$\sigma_Y^2(t) \cong 2e\Delta f m_X(t). \quad (108)$$

As shown by Eq. (B3),

$$m_{\hat{\sigma}_Y}(t) = \sigma_Y(t). \quad (109)$$

Thus from Eqs. (108) and (109) and Fig. 6

$$m_{Y_0}(t) \cong K m_{\hat{\sigma}_Y}(t) \cong K (2e\Delta f)^{1/2} m_X^{1/2}(t). \quad (110)$$

*It is simple to include one or more higher order terms in Eq. (97); however, the three-term expansion is sufficient to illustrate the point that slowly varying $m_X(t)$ can defeat the processor of Fig. 6 by inducing mean crossings.

In the remainder of this section

- We will assume that the transfer function $H(f)$ has a simple bandpass characteristic (to be given by Eq. (111)).
- We will assign the mean current $m_X(t)$ a waveshape many dwell times in duration, representative of an extended nontargetlike object in the sensor's field of view.
- We will evaluate Eqs. (107) and (110) for the mean filtered current $m_Y(t)$ and mean threshold $m_{Y_0}(t)$ respectively and will show that mean crossings occur (Eq. 42, Fig. 3a, and the accompanying discussion). Each such mean crossing is correctly interpreted as a false target report, that is, as a "false alarm."
- We will conclude that the Fig. 6 processor is not effective for suppressing false alarms from nonpointlike structural features in the background. The only current statistics required to make this assessment are $m_Y(t)$ and $m_{Y_0}(t)$; there is no need to calculate the other current statistics ($\sigma_Y, \sigma_{\dot{Y}}, \sigma_{Y_0}, \sigma_{\dot{Y}_0}$) or the threshold-crossing statistic \dot{m}_J . Thus the processor is operating in a basically nonstatistical regime: quantum-noise effects (as reflected in the magnitude of σ_Y for example) are totally overshadowed by background-structure effects. This operating regime, designated as the "background-structure-limited" (BSL) regime, has the characteristic that each false alarm that occurs can be associated with a structural feature in the background.

Model Filters and Backgrounds

We choose a form of "raised cosine" for the model-filter characteristic $H(f)$ (Fig. 7):

$$|H(f)| = \sin^2(\pi f_1/2f), \quad 0 \leq f \leq f_1, \quad (111a)$$

$$= 1, \quad f_1 \leq f \leq f_2, \quad (111b)$$

$$= \cos^2[\pi(f - f_2)/2(f_3 - f_2)], \quad f_2 \leq f \leq f_3, \quad (111c)$$

$$= 0, \quad f_3 \leq f. \quad (111d)$$

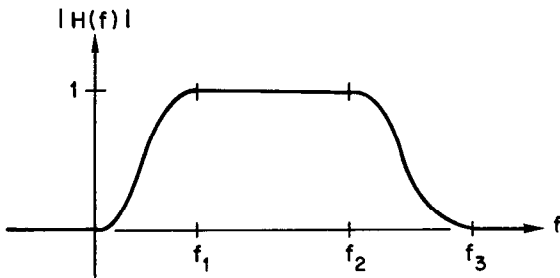


Fig. 7 — Modified raised-cosine model for the filter characteristic $H(f)$. Our illustrative numerical examples in this report all assume that $|H(f)|$ has the form depicted here. Analytic expressions for $|H(f)|$ and Δf appear as Eqs. (111) and (114). The analytic expression for $(\Delta f)_{rms}$ (Eq. (48)) is more complicated than Eq. (114) for Δf . However, the numerical value of $(\Delta f)_{rms}$ is usually not much different than the value of Δf .

It can be shown from Eqs. (111) that

$$H(0) = H'(0) = 0 \quad (112)$$

and

$$H''(0) = \pi^2/2f_1^2. \quad (113)$$

It follows from Eqs. (25) and (111) that the noise bandwidth of the model filter is

$$\Delta f = (5f_2 + 3f_3 - 5f_1)/8. \quad (114)$$

An analytical expression has been obtained for the rms bandwidth defined by Eq. (48) but is not given here.

Our model background, transformed from radiance to current by Eq. (A6), gives rise to a mean detected signal of the following parametric form:

$$m_X(t) = x_0\{1 + x_1[1 + (t/\tau)^2]^{-1}\}. \quad (115)$$

The parameters x_0 , τ , and x_1 correspond respectively to a constant background level, the halfwidth at half maximum of an "object" in the scene, and the object/background peak contrast. Depending on whether τ is large or small compared to the system dwell time (and the duration of $h(t)$), Eq. (115) for $m_X(t)$ is representative of a "clutterlike" or a "targetlike" object respectively. A representative plot of Eq. (115) is given in Fig. 8. For the present purposes we assume τ is much longer than a dwell time, so that $m_X(t)$ is definitely not targetlike.

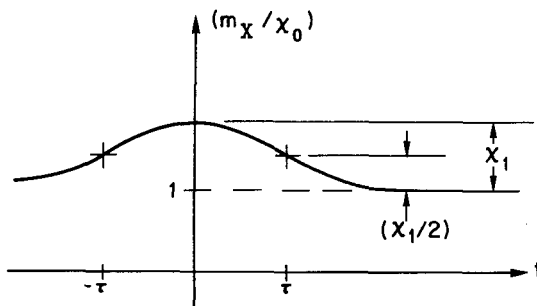


Fig. 8 — Model nonuniform background scene, transformed from radiance to average current by Eq. (A6). Our illustrative numerical examples in this report all assume that $m_X(t)$ has the form depicted here. An analytic expression for $m_X(t)$ appears as Eq. (115). The parameters x_0 , τ , and x_1 correspond respectively to a constant background level, the halfwidth at half maximum of an "object" in the scene, and the object/background peak contrast. Negative-contrast objects are modeled by choosing $x_1 < 0$. Depending on whether τ is large or small compared to the system dwell time, our model $m_X(t)$ is representative of a "clutterlike" or a "targetlike" object respectively.

From Eqs. (107), (113), and (115)

$$m_Y(t) \cong m_Y(0) [1 - 3(t/\tau)^2] [1 + (t/\tau)^2]^{-3}, \quad (116)$$

where

$$m_Y(0) = x_0 x_1 / 8 (f_1 \tau)^2. \quad (117)$$

From Eqs. (108) and (115)

$$\sigma_Y(t) \cong (2e \Delta f x_0)^{1/2} \{1 + x_1[1 + (t/\tau)^2]^{-1}\}^{1/2}, \quad (118)$$

with Δf being given by Eq. (114).

Figure 6 Processor

We see that for the Fig. 6 processor

$$Y_0(t) = K \hat{\sigma}_Y(t - T_d). \quad (119)$$

Taking the expected value of Eq. (119) and using Eq. (B3), we obtain

$$m_{Y_0}(t) = K \sigma_Y(t - T_d), \quad (120)$$

where σ_Y is given by Eq. (118) for the model filter and model background of the previous subsection.

Equations (116) and (120) are plotted in Fig. 9 with the illustrative parameter values

$$x_0 = 10^{-9} \text{ A}, \quad (121a)$$

$$x_1 = 1, \quad (121b)$$

$$\tau = 12.5 T_d \text{ s}, \quad (121c)$$

$$\Delta f = 5000 \text{ Hz}, \quad (122a)$$

$$f_1 = 2000 \text{ Hz}, \quad (122b)$$

$$(\Delta f)_{rms} = 4034 \text{ Hz}, \quad (122c)$$

and

$$K = 9. \quad (123)$$

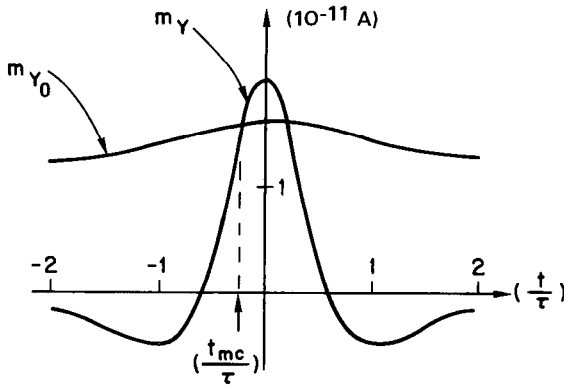


Fig. 9 — Illustrative calculations of the mean video m_Y and the mean threshold m_{Y_0} for the processor depicted in Fig. 6. Model background and filter parameters are as specified by Eqs. (121) through (124). It is assumed that the sensor is scanning an object 12.5 target widths in extent, which is an object far too large to be a target. This figure shows that the Fig. 6 processor experiences a mean crossing against the nontarget-like object, giving rise to a false alarm. Thus, the Fig. 6 processor is ineffective against spatially structured scenes.

From Eqs. (118), (121), and (122) the nominal rms sensor noise is

$$\sigma_Y(\infty) = (2e\Delta f x_0)^{1/2} = 1.27 \times 10^{-12} \text{ A}.$$

We calculate the peak contrast in our model background from Eqs. (115) and (121) as

$$[m_X(0) - m_X(\infty)] = x_0 x_1 = 1 \times 10^{-9} \text{ A}.$$

Thus the peak contrast in the background is

$$\frac{m_X(0) - m_X(\infty)}{\sigma_Y(\infty)} = 790$$

times larger than nominal noise-equivalent irradiance (NEI) of the sensor, for the parameter values we have chosen (Eqs. (121) and (122)). We assume the system dwell time is related to the noise bandwidth Δf by the usual search-set rule of thumb [10]

$$T_d = (2\Delta f)^{-1} = 10^{-4} \text{ s.} \quad (124)$$

According to Eqs. (121) and (124) the full width 2τ of the object represented by Eq. (115) is 25 dwell times in duration, and the signal from an unresolved target is about 2 dwell times in duration. Thus the size of the object represented by Eq. (115) is 12.5 target widths.

As may be seen directly from Fig. 9, the extended object represented by Eqs. (115), (121), and (124) does give rise to a mean crossing. Furthermore, as we discussed following Eq. (42), a mean crossing assures that a threshold crossing will occur. However, because the object under observation is about 12.5 target widths in extent, this threshold crossing must be interpreted as a false alarm.

In the next subsection we show that simple modifications to the structure of Fig. 6 result in a processor design that reliably discriminates between point objects and slowly varying extended objects, at the expense of some performance against uniform backgrounds.

Improved Processors

Inspection of Fig. 9 shows that the mean threshold $m_{Y_0}(t)$ derived by the Fig. 6 processor does not increase quickly enough or strongly enough to prevent a mean crossing. Prevention of this mean crossing requires that the mean threshold $m_{Y_0}(t)$ advance in synchrony with the mean current $m_Y(t)$.

An AT receiver structure with a more responsive threshold mechanism is shown in Fig. 10. Instead of Eq. (120), one now obtains

$$m_{Y_0}(t) = m_Y(t - T_d) + K\sigma_Y(t - T_d). \quad (125)$$

We set the delay time T_d in Eq. (125) and Fig. 10 equal to the sensor's dwell time. We presume that Eqs. (116) through (118) for m_Y and σ_Y are still valid.

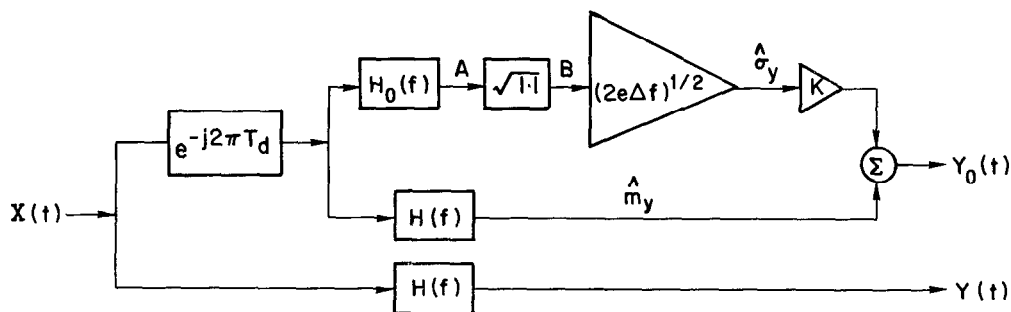


Fig. 10 — Candidate processor with a nonzero mean-video estimator. Comparison with Fig. 5 shows that the mean-video estimate is simply a time-delayed version of the video signal: $\hat{m}_Y(t) = Y(t - T_d)$. The rms noise estimate is the same as for the Fig. 6 processor, enabling this structure to achieve CFAR performance against all uniform scenes regardless of radiance. The time-delay element in the threshold circuit is required to prevent self-thresholding by a target waveform.

The performance of the Fig. 10 processor is most easily assessed by means of a numerical example. Once again we employ Eqs. (111) and (115) as parametric models for $H(f)$ and $m_Y(t)$ respectively with parameter values specified by Eqs. (121) through (124). The corresponding values of m_Y and m_{Y_0} are plotted as functions of time in Fig. 11a.

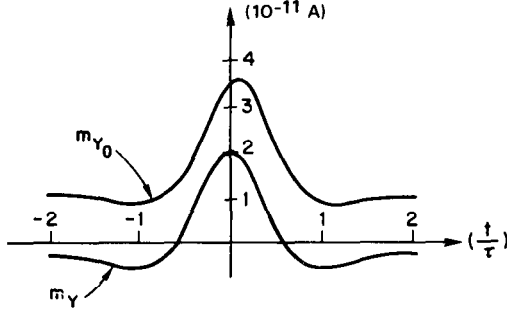


Fig. 11a — Illustrative calculations of the mean video m_Y and the mean threshold m_{Y_0} for the Fig. 10 processor. Model background and filter parameters are the same as for Fig. 9. The sensor is again assumed to scan an object $N = 12.5$ target widths in extent. Comparison with Fig. 9 shows that a considerable performance improvement has been achieved, since the mean crossing present in Fig. 9 has now been eliminated.

Comparison of Fig. 11a with Fig. 9 shows that a considerable performance improvement has been gained: the background-induced mean crossing (the certain false alarm) present in Fig. 9 has been eliminated. Figure 11a shows that the mean threshold $m_{Y_0}(t)$ appears to accurately track the mean current $m_Y(t)$.

However, a performance assessment based solely on visual inspection of Fig. 11a is incomplete and misleading. Once background-induced mean crossings are indicated (as in Fig. 9), the analysis need go no further: the performance of a grossly inadequate processor may be assessed quite simply, without need to evaluate either σ_{YY_0} or \dot{m}_J . However, the absence of mean crossings (as in Fig. 11a) is not necessarily indicative of adequate performance. We show this by calculating a 300-fold increase in the expected number of threshold crossings over the time interval $|t/\tau| \leq 2$ due to the presence of the nontargetlike object.

From Eqs. (41), (48), and (39)

$$m_J \equiv (\Delta f)_{rms} \int_I \exp[-u^2(t)/2] dt \quad (126)$$

for slowly varying scenes, where

$$u(t) = [m_{Y_0}(t) - m_Y(t)]/\sigma_{YY_0}(t). \quad (127)$$

From Eq. (37)

$$\sigma_{YY_0}^2(t) = \sigma_Y^2(t) + \sigma_{Y_0}^2(t). \quad (128)$$

The quantities $m_Y(t)$, $\sigma_Y(t)$, and $m_{Y_0}(t)$ are calculated from Eqs. (116), (118), and (125) respectively for the Fig. 10 processor. Evaluation of $m_J(t)$ by means of Eqs. (126) through (128) can now be performed, once it is shown how σ_{Y_0} is calculated.

From Eq. (60) and Fig. 10

$$Y_0(t) = \hat{m}_Y(t) + K \hat{\sigma}_Y(t), \quad (129)$$

where

$$\hat{m}_Y(t) = Y(t - T_d). \quad (130)$$

From Eq. (130)

$$\sigma_{\hat{m}_Y}(t) = \sigma_Y(t - T_d). \quad (131)$$

From Eqs. (131) and (B3)

$$\sigma_{\hat{m}_Y}(t) = m_{\hat{\sigma}_Y}(t - T_d). \quad (132)$$

From Eqs. (132) and (B6)

$$\sigma_{\hat{\sigma}_Y}(t)/\sigma_{\hat{m}_Y}(t) = \sigma_{\hat{\sigma}_Y}(t)/m_{\hat{\sigma}_Y}(t - T_d) = O(10^{-3}). \quad (133)$$

From Eqs. (129), (133), and (131)

$$\sigma_{Y_0}(t) \cong \sigma_{\hat{m}_Y}(t) = \sigma_Y(t - T_d). \quad (134)$$

Finally from Eqs. (128) and (134)

$$\sigma_{Y_0}^2(t) \cong \sigma_Y^2(t) + \sigma_Y^2(t - T_d), \quad (135)$$

where $\sigma_Y(t)$ and $\sigma_Y(t - T_d)$ are calculated from Eq. (118).

The quantity $u(t)$ given by Eq. (127) corresponding to Fig. 11a is plotted as Fig. 11b. If there is no object in the field of view, so that $x_1 = 0$ in Eq. (115), the expected number of false alarms during the time interval $|t/\tau| \leq 2$ is given by

$$m_J = (\Delta f)_{rms} 4\tau \cdot \exp(-K^2/4) = 3.2 \times 10^{-8}, \quad (136)$$

where the appropriate values for τ , $(\Delta f)_{rms}$, and K are obtained from Eqs. (121), (122), and (123) respectively. However, integrating Eq. (126) numerically with $u(t)$ as given by Fig. 11b, we find that

$$m_J = 1 \times 10^{-5}. \quad (137)$$

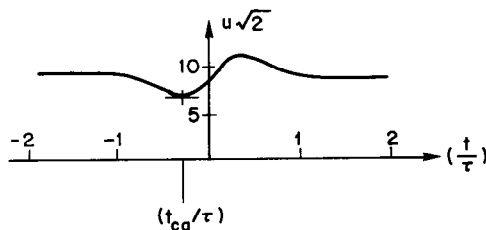


Fig. 11b — Illustrative calculations of $u(t) \equiv (m_{Y_0} - m_Y)/\sigma_{YY_0}$ for the same parameter values as used for Fig. 11a. The threshold-crossing rate increases about four orders of magnitude in the neighborhood of the closest-approach time t_{ca} . The false-alarm probability during a time interval $|t/\tau| \leq 2$, as calculated from Eq. (126), shows a 300-fold increase due to the presence of the nontargetlike object. Thus the time variation in $u(t)$ reflects less-than-ideal performance.

Comparison of Eqs. (137) and (136) shows that the probability of a false alarm has increased more than 300-fold. This is a significant deficiency in performance, since the full width of the object in the field of view is 12.5 times larger than a target.

We examine the variation in processor performance with object size by defining the parameter N as

$$N = (\tau/T_d). \quad (138)$$

Thus N is the ratio of object size to target size. In our preceding example we assumed a value $N = 12.5$ (Eq. (121c)). Plots of $u(t)$ for object sizes $N = 9$ and $N = 6.5$ are shown in Fig. 12. All parameter values other than τ are as specified by Eqs. (121) through (124).

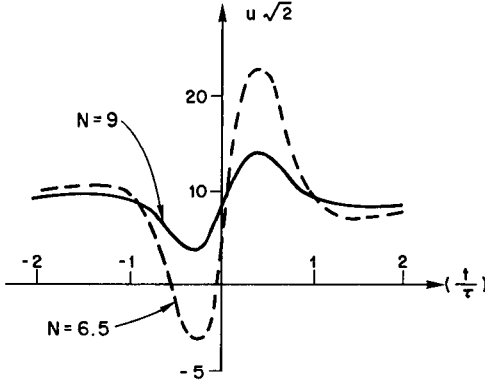


Fig. 12 — Plot which together with Fig. 11b shows the effect of object size on the performance of the Fig. 10 processor. All parameter values except for object size N are the same as in Fig. 11b. An object with size $N = 9$ target widths causes a six-order-of-magnitude increase in the nominal false-alarm probability during the time interval $|t/\tau| \leq 2$. As we discussed in the text, this is established by evaluating Eq. (126) for m_j with $u(t)$ as given by the solid ($N = 9$) curve in this figure. According to Eq. (139) a 6% false-alarm probability is calculated for the 9-target-width object. The zero intercept for $N=6.5$ indicates a mean crossing. Hence the Fig. 10 processor suffers a certain false alarm against an object 6.5 target widths in extent.

The $N = 9$ curve in Fig. 12 shows even more dramatically than for $N = 12.5$ that the absence of mean crossings is not indicative of adequate performance. The threshold-crossing rate, as calculated from Eq. (126), briefly increases by seven orders of magnitude as the sensor is scanned across the nontargetlike object 9 times larger than a target. The probability of a quantum-noise-induced threshold crossing, originally small, grows to significant amplitude in the neighborhood of the time at which the difference between m_{Y_0} and m_Y assumes its minimum value (the "time of closest approach").

Integrating Eq. (126) numerically with $u(t)$ as given by the $N = 9$ curve in Fig. 12, we find

$$m_j = 0.06, \quad N = 9, \quad (139)$$

corresponding to a 6% probability of false alarm. If there were no object in the field of view, so that $x_1 = 0$ in Eq. (115), the expected number of false alarms during the time interval $|t/\tau| \leq 2$ is obtained from Eq. (136) as

$$m_j = (9/12.5) \times 3.2 \times 10^{-8} = 2.3 \times 10^{-8}. \quad (140)$$

The factor $9/12.5$ in Eq. (140) is due to the linear dependence of m_j on τ (Eq. (136)), and the linear variation of τ with N (Eq. (138)). Comparison of Eqs. (139) and (140) shows that the extended object, 9 target widths wide, has caused a six-order-of-magnitude increase in the false alarm probability.

The dashed curve in Fig. 12 shows that the Fig. 10 processor suffers a mean crossing (and hence a certain false alarm) for $N = 6.5$, that is, for objects 6.5 times larger than a target. Clearly there is still considerable room for improvement in processor performance.

Improved performance is obtained with the processor structure depicted in Fig. 13. The transfer function $H_0(f)$ in Fig. 13 is related to $H(f)$ as follows (Eq. (B1)):

$$H_0(f) = (2\Delta f)^{-1} H(f) \otimes H(f), \quad (141)$$

corresponding to an impulse response

$$h_0(t) = (2\Delta f)^{-1} h^2(t), \quad (142)$$

where $h(t)$ and $h_0(t)$ are the Fourier transforms of $H(f)$ and $H_0(f)$ respectively.

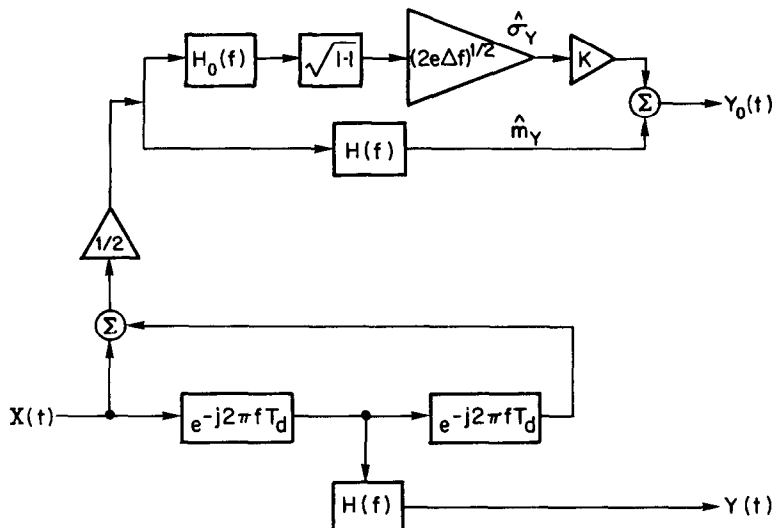


Fig. 13 — Candidate adaptive-threshold signal-processing structure. The estimated value of the mean video \hat{m}_Y is obtained as the average of time-delayed and time-advanced versions of the video, as we will give as Eq. (143). Since the quantity $\hat{m}_Y(t) - Y(t)$ is proportional to the discrete-time second derivative of $Y(t)$, this processor is a Laplacian linear spatial filter, modified to incorporate the "efficient shot noise estimator" developed in Appendix B.

From inspection of Fig. 13 and Eq. (142) the mean and variance estimates are obtained as

$$\hat{m}_Y(t) = [Y(t - T_d) + Y(t + T_d)]/2 \quad (143)$$

and

$$\hat{\sigma}_Y^2(t) = e h^2(t) \otimes [X(t - T_d) + X(t + T_d)]/2. \quad (144)$$

It can be shown from Eqs. (143) and (144) that

$$m_{Y_0}(t) = \frac{1}{2}(m_Y^- + m_Y^+) + K \left[\frac{1}{2}(\sigma_Y^{2+} + \sigma_Y^{2-}) \right]^{1/2} \quad (145)$$

and

$$\sigma_{Y_0}^2(t) = \sigma_Y^2(t) + \frac{1}{2}(\sigma_Y^{2-} + \sigma_Y^{2+}), \quad (146)$$

where

$$\sigma_Y^{\pm} \equiv \sigma_Y(t \pm T_d) \quad (142a)$$

and

$$m_Y^{\pm} \equiv m_Y(t \pm T_d). \quad (147b)$$

Again we examine the performance of our latest candidate processor structure by considering some numerical examples. If the model filter and model background are again assumed to be given by Eqs. (111) and (115) respectively, $m_Y(t)$ and $\sigma_Y(t)$ are still given by Eqs. (116) and (118). Equations (126), (127), and (128) for m_J , $u(t)$, and $\sigma_{YY_0}(t)$ are also still applicable. However, Eqs. (145) and (146) now replace Eqs. (125) and (135) respectively.

The first set of numerical calculations for the Fig. 13 processor is shown in Fig. 14, where all parameter values except for τ are as specified by Eqs. (121) through (124). Values of τ for Fig. 14 are given by

$$\tau = NT_d, \quad N = 5, 6.5, 9, \quad (148)$$

where $T_d = 10^{-4}$ s, as given by Eq. (124). When m_J is calculated by means of Eq. (126), the result for the expected number of false alarms during the interval $|t/\tau| \leq 2$ is

$$m_J = 9.4 \times 10^{-7}, \quad N = 9, \quad (149)$$

corresponding to the solid curve ($N = 9$) in Fig. 14.

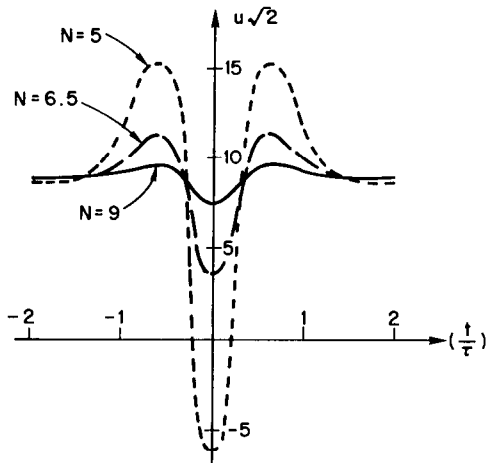


Fig. 14 — Performance assessment of the Fig. 13 processor against objects of various sizes. All parameters except for object size are the same as for Figs. 11 and 12. The processor experiences no difficulty in suppressing false alarms for $N = 9$ (against the 9-target-width object), retains marginal capability for $N=6.5$, and experiences a certain false alarm for $N=5$.

Comparison of Eqs. (149) and (139) shows that the false-alarm probability of the Fig. 13 processor is about five orders of magnitude smaller than the false-alarm probability of the Fig. 10 processor. This is an important improvement in performance. Further comparison, of Figs. 12 and 14, shows that the Fig. 10 processor suffers a certain false alarm (a mean crossing) for $N = 6.5$, but the Fig. 13 processor does not. However, inspection of Fig. 14 shows that the Fig. 13 processor suffers a certain false alarm for $N = 5$ (for an object 5 times wider than a target). Again the latest processor (Fig. 13) has considerable room for improvement as a detector of unresolved targets.

Noise Bandwidth and Dwell Time

In this subsection we will show that system performance against nonuniform scenes can be improved at the expense of degraded performance against uniform scenes. We presume that the signal processor is structured as in Fig. 13.

The key to improving this processor's performance against extended (nontargetlike) objects is to modify the conventional search-set rule of thumb relating noise bandwidth and dwell time [10] as given by Eq. (124):

$$\Delta f = (2T_d)^{-1}. \quad (150)$$

We now consider the effect on system performance of choosing a value for Δf four times larger than specified by Eq. (150):

$$\Delta f = M(2T_d)^{-1}, \quad M = 4. \quad (149)$$

We refer to the processor described by Eq. (150) and Fig. 13 as an " $M=1$ processor" or "narrowband processor," and we refer to the processor described by Eq. (151) and Fig. 13 as an " $M=4$ processor" or "wide-band processor." We evaluate the relative performance of the two processors by extending the numerical example of the previous subsection.

We calculate Fig. 15 by means of the same equations as Fig. 14, except that we employ the following parameter values (descriptive of the $M=4$ processor) instead of Eqs. (121) through (124):

$$x_0 = 10^{-9} \text{ A}, \quad (152a)$$

$$x_1 = 1, \quad (152b)$$

$$\tau = NT_d, \quad N = 2.5, 5, \quad (152c)$$

$$\Delta f = 20 \text{ kHz}, \quad (153a)$$

$$f_1 = 8 \text{ kHz}, \quad (153b)$$

$$(\Delta f)_{rms} = 16.136 \text{ kHz}, \quad (153c)$$

and

$$K = 9. \quad (154)$$

From Eqs. (151) and (153)

$$T_d = 10^{-4} \text{ s}; \quad (155)$$

that is, the sensor dwell time is the same as for the previous example (Eq. (124)).

Comparison of Figs. 14 and 15 shows that the $M=1$ processor suffers a certain false alarm while the performance of the $M=4$ processor is barely perturbed for an object 5 target widths in size ($N=5$). Further inspection of Fig. 15 shows that the $M=4$ processor retains some capability even against extended objects just 2.5 target widths in size.* Increasing the noise bandwidth still further, by choosing $M > 4$ in Eq. (151), results in even greater selectivity against extended targets.

*We cannot evaluate sensor performance using the approximate Eqs. (116) and (118) for smaller values of N due to our slowly-varying-background approximation, Eq. (98). This limitation is due to our desire to maintain computational simplicity in our numerical examples and is not fundamental to the theory.

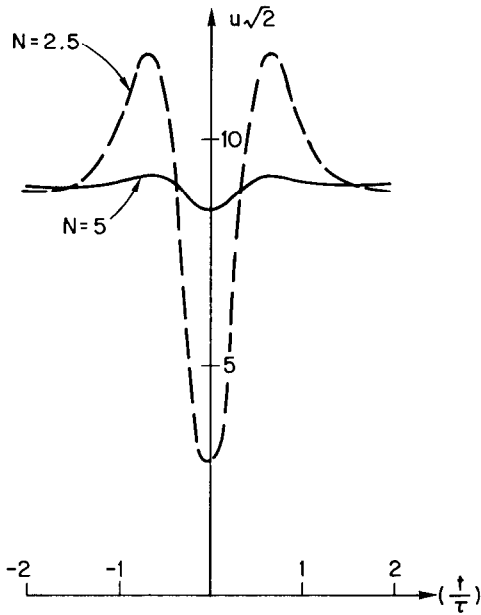


Fig. 15 — Performance assessment of the Fig. 13 processor employing a wide-bandwidth electrical filter. The noise bandwidth for this figure is 4 times larger than for Fig. 14. Processor performance is barely perturbed by the presence of the same 5-target-width object ($N=5$) that would cause the narrow-bandwidth ($M=1$) processor to experience a false alarm (Fig. 14). The wide-bandwidth ($M=4$) processor retains marginal capability against an $N=2.5$ target-width object. The improvement in performance against nonuniform scenes for the $M=4$ processor compared to the $M=1$ processor is gained at the expense of degraded performance against uniform scenes.

We now show that the improvement in performance against nonuniform scenes for values $M > 1$ is gained at the expense of degraded performance against uniform scenes.

With the assumption that $H(f)$ in Fig. 13 is a bandpass characteristic, it follows from Eqs. (82) and (147) that for uniform backgrounds

$$m_Y^+ = m_Y^- = 0, \quad (156a)$$

and

$$\sigma_Y^+ = \sigma_Y^- \equiv \sigma_Y. \quad (156b)$$

Thus, from Eqs. (145) and (156)

$$m_{Y_0} = K \sigma_Y \quad (157)$$

against unstructured scenes (for which $x_1 = 0$ in Eq. (115)). Also, from Eqs. (118) and (115) (with $x_1 = 0$), we find

$$\sigma_Y = (2ex_0\Delta f)^{1/2}. \quad (158)$$

Thus, from Eqs. (157), (158), and (151)

$$m_{Y_0} \propto K(\Delta f)^{1/2} \propto K M^{1/2}. \quad (159)$$

According to Eq. (159) the threshold value m_{Y_0} for the $M=4$ processor is twice as large as the mean threshold for the $M=1$ processor. Consequently the peak target signal strength must be twice as great to induce a mean crossing (a certain target detection) in the $M=4$ processor than in the $M=1$ processor.*

*The structure of the Fig. 13 processor ensures that a target signal does not experience significant self-thresholding.

Alternatively it follows from Eq. (159) that we can compensate for a 4-fold increase in Δf by halving the threshold gain K . Instead of Eq. (154), the equations

$$\begin{aligned} K &= 9/2, \quad M = 4, \\ &= 9, \quad M = 4, \end{aligned} \quad (160)$$

assure that the $M=4$ and $M=1$ processors have equal values of m_{y_0} and hence equal values of target signal strength required to induce a certain target detection.

From Eqs. (8), (126), (127), (128), (145), (146), and (156)

$$\text{FAR} \propto \exp(-K^2/4) \quad (161)$$

for the Fig. 13 processor, for operation against uniform scenes. It follows from Eqs. (160) and (161) that the reduced value of threshold gain required to equalize target-detection probabilities results in a greatly degraded uniform-background false-alarm rate for the $M=4$ processor as compared with the $M=1$ processor.

Analogous to our discussion following Eq. (52) the performance disadvantage described can be interpreted as a uniform-background false-alarm-penalty (FAP) that accrues to the use of wide-bandwidth processors ($M > 1$). For the Fig. 13 processor we can show that

$$\text{FAP}(M) = 1.086 K^2(1 - M^{-1}) \text{ dB}. \quad (162)$$

For the previous numerical example ($K = 9$, $M = 4$) we find

$$\text{FAP} = 66 \text{ dB}.$$

Table 2 summarizes the results of our numerical examples.

The Promise of Focal-Plane-Array Technology

The performance disadvantage incurred by quadrupling Δf (as we pointed out following Eq. (161)) can be completely offset by replacing each detector element with four series TDI detectors (as determined by equations similar to Eqs. (58) and (59) in the subsection "Time Delay and Integration"). Thus, improvements in focal-plane-array (FPA) technology [15] leading to large numbers of TDI elements may afford us "excess" uniform-background sensitivity that we can intentionally sacrifice in the interest of better performance against structured backgrounds.

Table 2 — Summary of performance calculations of candidate processors. In performing example calculations, we assume that the filter characteristic and background variation have the parametric forms indicated in Eqs. (111) and (115) respectively. All calculations assume numerical values for the parameters x_0 , x_1 , K , and T_d given by Eqs. (121), (123), and (124). Calculations for narrow-bandwidth electrical filters, Eqs. (122), correspond to the bandwidth parameter $M = 1$, and calculations for wide bandwidth filters correspond to Eqs. (153) and $M = 4$. The parameter N is the ratio of object size to target size. Object contrast relative to sensor noise-equivalent irradiance (NEI) is equal to 790 for the $M=1$ calculations, and 395 for the $M=4$ calculations. The minimum target signal strength required to assure target detection is 9 times the sensor NEI for all calculations. The last entry in the table ($N = 2.5$, $M = 4$) indicates that a clutter object 2.5 target widths in extent and of amplitude $395/9 = 44$ times greater than the minimum target contrast required for assured detection gives rise to a 12% probability of false alarm.

Processor	Object Size N	Bandwidth M	False-Alarm Probability, $ t/\tau \leq 2$	
			Nominal	Degraded
Fig. 6	12.5	1	5.2×10^{-17}	1
Fig. 10	12.5	1	3.2×10^{-8}	1×10^{-5}
	9.	1	2.3×10^{-8}	6×10^{-2}
	6.5	1	1.7×10^{-8}	1
Fig. 13	9.	1	2.3×10^{-8}	9.4×10^{-7}
	6.5	1	1.7×10^{-8}	3.5×10^{-2}
	5.	1	1.3×10^{-8}	1
Fig. 13	5	4	5.2×10^{-8}	8.2×10^{-8}
	2.5	4	2.6×10^{-8}	1.2×10^{-1}

Appendix A

CALCULATING THE AVERAGE CURRENT FROM BACKGROUND DATA

Our objective in this appendix is to derive Eq. (A5), which expresses the average value of the random current $X(t)$ (Fig. 1)

$$m_X(t) \equiv E\{X(t)\} \quad (\text{A1})$$

as a function of the scene radiance m_L and a number of important sensor parameters. We will derive Eq. (A5) subject to the assumptions that the scene is spatially uniform (that the radiance m_L is independent of view angle) and that the average current m_X is constant with time. We will then generalize Eq. (A5) to Eq. (A6) to allow for the possibility of spatially nonuniform background radiances and time-variable average currents $m_X(t)$.

The average value of the photocurrent $X(t)$ (Fig. 1) may be calculated as

$$m_X = \eta e m_Q, \quad (\text{A2})$$

where m_X is defined by Eq. (A1), η is the quantum efficiency of the detector [electrons per photon], e is the electronic charge [coulombs per electron], and m_Q is the average photon flux incident on the detector [photons per second]. The quantities m_X and m_Q in Eq. (A2) are both averages over the photon fluctuation statistics of the incident light. The meaning of the ensemble averaging process in the present context is discussed in Part I [1]; in particular, the average in Eq. (A1) is *not* a time average.

The mean photon flux incident on the detector, m_Q in Eq. (A2), is given by

$$m_Q = A_{\text{det}} m_E / h\nu, \quad (\text{A3})$$

where A_{det} is the active area of the photodetector [cm^2], m_E is the focal-plane irradiance [$\text{W}\cdot\text{cm}^{-2}$], and $h\nu$ is the radiant energy [J] per photon.

The focal-plane irradiance m_E in Eq. (A3) is calculated as

$$m_E = \pi \tau_o m_L / (2f^\#)^2 \equiv K_o m_L, \quad (\text{A4})$$

where τ_o is the transmittance of the optics [dimensionless], $f^\#$ is the focal-length ratio of the optics [dimensionless], and m_L is the radiance of the scene [$\text{W}\cdot\text{cm}^{-2}\cdot\text{sr}^{-1}$].

It follows from Eqs. (A2) through (A4) that

$$m_X = K_o R_I A_{\text{det}} m_L \quad (\text{A5})$$

where the current responsivity R_I is defined as $= \eta e / h\nu$ [$\text{A}\cdot\text{W}^{-1}$]. Equation (A5) is valid for only uniform backgrounds that fill the sensor's field of view. Nonuniform backgrounds can be characterized in terms of a radiance distribution

$$m_L(\theta) \equiv m_L(\alpha, \beta),$$

where α and β are azimuth and elevation angles respectively. The appropriate generalization of Eq. (A5) when the background is nonuniform is [1]

$$m_X(t) = K_o R_I \int \text{MTF}(\mathbf{f}) \mathcal{P}(\mathbf{f}) m_g(\mathbf{f}) e^{(j2\pi\mathbf{f} \cdot \mathbf{v}t)} d\mathbf{f}, \quad (\text{A6})$$

where

\mathbf{f} = two-dimensional spatial frequency $[(\text{cycles} \cdot \text{cm}^{-1})^2]$,

$\text{MTF}(\mathbf{f})$ = modulation transfer function of the optical train [dimensionless],

\mathbf{v} = focal-plane scan velocity $[\text{cm} \cdot \text{s}^{-1}] = 2\pi d / T_F$,

d = focal length of the optics [cm],

T_F = system frame time [s],

and $P(\mathbf{f})$ and $m_L(\mathbf{f})$ are the two-dimensional Fourier transforms of the quantities $P(\mathbf{r})$ and $m_L(-\mathbf{r}/d)$:

$$\mathcal{P}(\mathbf{f}) = \int P(\mathbf{r}) \exp(j2\pi\mathbf{f} \cdot \mathbf{r}) d\mathbf{r} \quad (\text{A7})$$

and

$$m_g(\mathbf{f}) = \int m_L(-\mathbf{r}/d) \exp(j2\pi\mathbf{f} \cdot \mathbf{r}) d\mathbf{r}, \quad (\text{A8})$$

where \mathbf{r} is the two-dimensional focal-plane location vector [cm]. For the detector geometry depicted in Fig. A1, the quantity $P(\mathbf{r})$ in Eq. (A7) is defined as

$$P(\mathbf{r}) = 1, \quad \mathbf{r} \in \mathcal{Q}_{\text{det}}, \quad (\text{A9a})$$

$$= 0, \quad \mathbf{r} \notin \mathcal{Q}_{\text{det}}. \quad (\text{A9b})$$

It follows from Eqs. (A7) and (A9) that

$$\mathcal{P}(\mathbf{0}) = A_{\text{det}} [\text{cm}^2]. \quad (\text{A10})$$

For uniform backgrounds

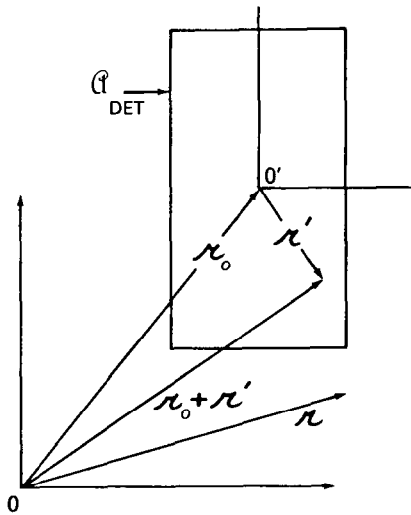


Fig. A1 — Focal-plane geometry. The focal-plane irradiance is stationary in the coordinate system with origin O. Vector \mathbf{r}_o locates the center of a detector of area A_{det} . For scanning sensors \mathbf{r}_o is a function of time.

$$m_x(\mathbf{f}) = m_L \delta(\mathbf{f}), \quad (\text{A11})$$

where $\delta(\cdot)$ is the Dirac delta function. From Eqs. (A6), (A10), (A11), and the conventional MTF normalization,

$$\text{MTF}(\mathbf{0}) = 1, \quad (\text{A12})$$

it follows that

$$m_X = K_o R_I A_{\text{det}} m_L \quad (\text{A13})$$

for uniform backgrounds. Equation (A13) is consistent with Eq. (A5), as expected. Finally, we note that the quantities $m_L(\boldsymbol{\theta})$ and $m_x(\mathbf{f})$, like $m_X(t)$, are defined as ensemble averages over the photon fluctuation statistics of the incident light.

Appendix B

EFFICIENT ESTIMATORS FOR NONSTATIONARY SHOT NOISE

INTRODUCTION

A main result of this report is the proposal of a new signal processor structure for generating high-confidence estimates of the time-varying rms quantum noise induced in a background-limited (BLIP) sensor as it scans a nonuniform scene. This new signal-processing structure has the general form illustrated in Fig. B1. For reasons that we will explain shortly, the processor depicted in Fig. B1 is called an "efficient shot-noise" (ESN) estimator.

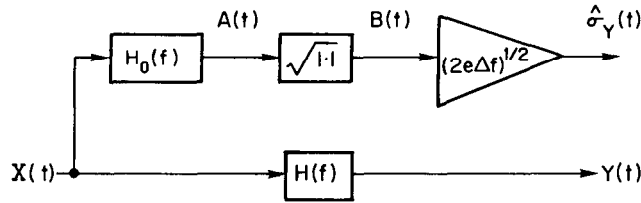


Fig. B1 — Efficient estimator for nonstationary shot noise. The transfer functions $H(f)$ and $H_0(f)$ are related by Eq. (B1). Realization of $H_0(f)$ requires either true dc response or dc restoration (Eq. B2). An important feature of this processor is that the expected value of $\hat{\sigma}_Y$ is equal to the rms value of $Y(t)$ (Eq. B3). All of the candidate processors in this report use the structure shown here to perform the rms quantum-noise estimation function indicated in Fig. 5.

The quantity $\hat{\sigma}_Y(t)$ in Fig. B1 is an estimate for the rms value of the random process $Y(t)$; that is, $\hat{\sigma}_Y(t)$ is an estimate for $\sigma_Y(t)$. Inspection of Fig. B1 shows that $\hat{\sigma}_Y$ is established by cascading a linear filter $H_0(f)$ with a square-root device and an amplifier of gain $(2e\Delta f)^{1/2}$. The frequency characteristic $H_0(f)$ is given by

$$H_0(f) = (2\Delta f)^{-1} H(f) \otimes H(f), \quad (\text{B1})$$

where \otimes is the convolution operator (Eq. (10)). Also, e is the electronic charge (1.6×10^{-19} C) and Δf is the noise bandwidth of $H(f)$, as defined by Eq. (25). The transfer function $H_0(f)$ given by Eq. (B1) is always a low-pass function. From Eqs. (25) and (B1)

$$H_0(0) = \max_f H_0(f) = 1. \quad (\text{B2})$$

Thus, realization of $H_0(f)$ always requires a sensor with either true dc response or dc restoration [11,12].

The noise estimate $\hat{\sigma}_Y$ established by the Fig. B1 processor, like $X(t)$ and $Y(t)$, is a random process. We show in this appendix that

$$m_{\hat{\sigma}_Y}(t) \equiv E\{\hat{\sigma}_Y(t)\} = \sigma_Y(t), \quad (\text{B3})$$

where $E\{\cdot\}$ denotes an ensemble average over the photon-fluctuation statistics of the incident light [1]. Equation (B3) indicates that the ensemble average value of the noise estimate $\hat{\sigma}_Y$ is equal to the actual rms noise σ_Y ; that is, that $\hat{\sigma}_Y$ is an "unbiased" estimate for σ_Y . Even so, $\hat{\sigma}_Y$ might assume a sufficiently large spread of values about its average to make $\hat{\sigma}_Y$ a poor estimate for σ_Y . To ensure that $\hat{\sigma}_Y$ is not a poor estimate, we calculate the mean-square estimation error:

$$\sigma_{\hat{\sigma}_Y}^2 \equiv E\{(\hat{\sigma}_Y - \sigma_Y)^2\}. \quad (\text{B4})$$

We show in this appendix that

$$\sigma_{\hat{\sigma}_Y}^2 = e^2 \Delta f \Delta f_0 \quad (\text{B5})$$

for the Fig. B1 processor, where e is the electronic charge, Δf is the noise bandwidth of $H(f)$, and Δf_0 is the noise bandwidth of $H_0(f)$ (Eq. (B1)).

It follows from Eq. (B3) that $\hat{\sigma}_Y(t)$ is generally a nonstationary random process, since the mean value of $\hat{\sigma}_Y$ is generally nonconstant with time. It is thus surprising to see from Eq. (B5) that the variance of $\hat{\sigma}_Y$ is time independent.

It follows from Eqs. (B5) and (B3) and from looking ahead to Eqs. (C4) through (C6) that the *relative* mean-square estimation error of the Fig. B1 processor is extremely small:

$$(\sigma_{\hat{\sigma}_Y}/m_{\hat{\sigma}_Y})^2 = (\sigma_{\hat{\sigma}_Y}/\sigma_Y)^2 = O(10^{-6}). \quad (\text{B6})$$

According to Eq. (B6) the variance of $\hat{\sigma}_Y$ is six orders of magnitude smaller than the variance of $Y(t)$. This results in significant simplifications in some of the analysis (as we will show following Eq. (95) for example.)

One commonly used approach to evaluating the effectiveness of an estimator invokes the Cramér-Rao inequality, which provides a lower bound on $\sigma_{\hat{\sigma}_Y}^2$ [4]. We evaluate the Cramér-Rao lower bound for $\sigma_{\hat{\sigma}_Y}^2$ in this appendix and show it to equal $\sigma_{\hat{\sigma}_Y}^2$ as given by Eq. (B5). Consistent with the conventional terminology of statistics, it follows that the Fig. B1 processor establishes an "efficient" estimate for σ_Y .

Before proceeding with the statistical arguments described, we will first show that the discrete-time implementation of Fig. B1 takes the particularly simple form shown in Fig. B2. The quantity T_d in Fig. B2 is both the dwell time of the sensor and the integration/sample time of the postdetector filter.

DISCRETE-TIME IMPLEMENTATION OF THE ESN ESTIMATOR

We now assume that the postdetector filter is simply an integrate, sample, and hold device. The waveform at the output of the postdetector filter is the discrete-time random process $W(k)$, where

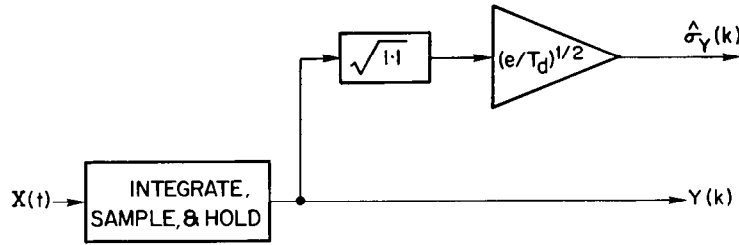


Fig. B2 — Discrete-time implementation of the efficient shot-noise estimator. The generic structure depicted in Fig. B1 simplifies considerably when it is implemented as a discrete-time device, since we now have $H(f) = H_0(f)$. The quantity T_d is both the dwell time of the sensor and the integration/sample time of the postdetector filter.

$$W(k) = T_d^{-1} \int_{(k-1/2)T_d}^{(k+1/2)T_d} X(\tau) d\tau. \quad (\text{B7})$$

With the function $\text{rect}(\cdot)$ defined as shown in Fig. B3 [13], Eq. (B7) can be written as

$$W(k) \equiv Y(kT_d), \quad (\text{B8})$$

where

$$Y(t) = T_d^{-1} \text{rect}(t/T_d) \otimes X(t). \quad (\text{B9})$$

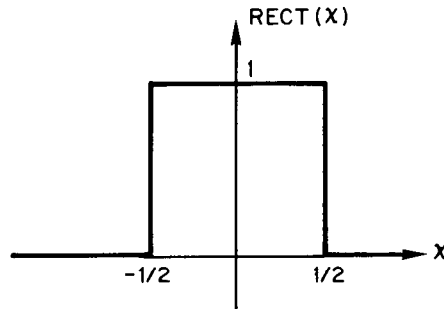


Fig. B3 — Definition of the function $\text{rect}(x)$. The impulse response of the postdetector filter is a scaled version of $\text{rect}(x)$ when the Fig. B1 processor is implemented in discrete time (Eq. (B9)).

Comparing Eqs. (10) and (B9), we see that the impulse response of the postdetector filter is

$$h(t) = T_d^{-1} \text{rect}(t/T_d). \quad (\text{B10})$$

Taking the Fourier transform of Eq. (B10), we obtain [13]

$$H(f) = \text{sinc}(fT_d) \equiv (\pi fT_d)^{-1} \sin(\pi fT_d). \quad (\text{B11})$$

It follows from Eq. (B11) that $H(f)$ is normalized properly (Eq. (24)):

$$H(0) = \max_f H(f) = 1. \quad (\text{B12})$$

Thus, from Eqs. (21), (25), and (B10),

$$\Delta f = (2T_d)^{-1}. \quad (\text{B13})$$

In addition it follows from Eqs. (142), (B10), and (B13) that

$$h_0(t) = h(t). \quad (\text{B14})$$

Finally it follows from Eqs. (B13) and (B14) that the discrete-time implementation of Fig. B1 takes the particularly simple form depicted in Fig. B2.

ESTIMATOR BIAS

Our purpose in this section is to show that

$$E\{\hat{\sigma}_Y - \sigma_Y\} = 0. \quad (\text{B15})$$

According to Eq. (B15) the mean estimation error is zero, so that $\hat{\sigma}_Y$ provides an unbiased estimate for σ_Y .

It follows from Fig. B1 that

$$\hat{\sigma}_Y(t) = (2e\Delta f)^{1/2} B(t). \quad (\text{B16})$$

Taking the expected value of both sides of Eq. (B16), we obtain

$$m_{\hat{\sigma}_Y} = (2e\Delta f)^{1/2} m_B. \quad (\text{B17})$$

From Eq. (B17) and the relation $m_B = m_A^{1/2} (1 - \epsilon)$, which we will give as Eq. (C40), where $\epsilon = (1/2) (\sigma_A/2m_A)^2$, which we will give as Eq. (C42),

$$m_{\hat{\sigma}_Y} = (2e\Delta f m_A)^{1/2} (1 - \epsilon). \quad (\text{B18})$$

It follows from inspection of Fig. B1 that

$$A(t) = h_0(t) \otimes X(t), \quad (\text{B19})$$

where \otimes is the convolution operator and $h_0(t)$ is the Fourier inverse of $H_0(f)$:

$$h_0(t) = F^{-1}\{H_0(f)\}. \quad (\text{B20})$$

It can be shown from Eqs. (B1) and (B20) and the convolution theorem for Fourier transforms that

$$h_0(t) = (2\Delta f)^{-1} h^2(t). \quad (\text{B21})$$

Thus from Eqs. (B19) and (B21)

$$A(t) = (2\Delta f)^{-1} h^2(t) \otimes X(t). \quad (\text{B22})$$

Taking the expected value of both sides of Eq. (B22), we find

$$m_A(t) = (2\Delta f)^{-1} h^2(t) \otimes m_X(t). \quad (\text{B23})$$

Substituting Eq. (B23) into Eq. (B18), we obtain

$$m_{\hat{\sigma}_Y}(t) = [eh^2(t) \oplus m_X(t)]^{1/2} (1 - \epsilon). \quad (\text{B24})$$

However, from Eq. (29)

$$\sigma_Y^2(t) = eh^2(t) \oplus m_X(t). \quad (\text{B25})$$

Thus from Eqs. (B24) and (B25)

$$m_{\hat{\sigma}_Y}(t) = \sigma_Y(t)(1 - \epsilon), \quad (\text{B26})$$

or

$$\frac{\sigma_Y - m_{\hat{\sigma}_Y}}{\sigma_Y} = \epsilon = O(10^{-6}). \quad (\text{B27})$$

According to Eq. (B27) the mean estimation error for σ_Y is six orders of magnitude smaller than σ_Y itself. The Fig. B1 processor is thus described as an asymptotically unbiased estimator for σ_Y .

MEAN-SQUARE ESTIMATION ERROR

In deriving Eq. (B5) we first note that

$$\sigma_{\hat{\sigma}_Y}^2 \equiv E\{(\hat{\sigma}_Y - \sigma_Y)^2\} = E\{\hat{\sigma}_Y^2\} + \sigma_Y^2 - 2\sigma_Y E\{\hat{\sigma}_Y\}. \quad (\text{B28})$$

It follows from Eq. (B26) that

$$E\{\hat{\sigma}_Y\} \equiv m_{\hat{\sigma}_Y} = \sigma_Y(1 - \epsilon), \quad (\text{B29})$$

where again, as we will give as Eq. (C42),

$$\epsilon = \frac{1}{2}(\sigma_A/2m_A)^2. \quad (\text{B30})$$

Since from Fig. B1

$$\hat{\sigma}_Y^2(t) = 2e\Delta f A(t), \quad (\text{B31})$$

it follows from Eq. (B22) that

$$\hat{\sigma}_Y^2(t) = eh^2(t) \oplus X(t). \quad (\text{B32})$$

From Eq. (B32)

$$\begin{aligned} E\{\hat{\sigma}_Y^2(t)\} &= e h^2(t) \oplus E\{X(t)\} \\ &\equiv e h^2(t) \oplus m_X(t). \end{aligned} \quad (\text{B33})$$

From Eqs. (B33) and (B25)

$$E\{\hat{\sigma}_Y^2(t)\} = \sigma_Y^2(t). \quad (\text{B34})$$

From Eqs. (B28), (B29), and (B34)

$$\sigma_{\hat{\sigma}_Y}^2 = 2 \epsilon \sigma_Y^2. \quad (\text{B35})$$

Since, as we will give as Eq. (C6), $\sigma_A/m_A = O(10^{-3})$, it follows from Eqs. (B35) and (B30) that

$$(\sigma_{\hat{\sigma}_Y}/\sigma_Y)^2 = O(10^{-6}), \quad (\text{B36})$$

verifying Eq. (B6).

From Eqs. (B30), (B23), (B25), and equations we will derive as Eqs. (C40) through (C43)

$$2\epsilon = e^2 \Delta f \Delta f_0 / \sigma_Y^2. \quad (\text{B37})$$

Equation (B5), which is one of the principal results of this appendix, now follows from Eqs. (B35) and (B37):

$$\sigma_{\hat{\sigma}_Y}^2 = e^2 \Delta f \Delta f_0. \quad (\text{B38})$$

CRAMER-RAO INEQUALITY

As shown by Van Trees [4, p. 66], the mean-square estimation error defined by Eq. (B4) must satisfy the Cramér-Rao inequality

$$\sigma_{\hat{\sigma}_Y}^2 \geq \sigma_{CRLB}^2. \quad (\text{B39})$$

The Cramér-Rao lower bound σ_{CRLB}^2 is defined as

$$\sigma_{CRLB}^2 \equiv -E\{\partial_{\sigma_Y, \sigma_Y}^2 \ln f_{\hat{\sigma}_Y|\sigma_Y}(\hat{\sigma}_Y|\sigma_Y)\}, \quad (\text{B40})$$

where $\partial_{\sigma_Y, \sigma_Y}^2$ denotes the second partial derivative with respect to σ_Y and $f_{\hat{\sigma}_Y|\sigma_Y}(\hat{\sigma}_Y|\sigma_Y)$ is the probability density function for $\hat{\sigma}_Y$ conditioned on σ_Y . Since $\hat{\sigma}_Y$ is obtained as the square root of a Gaussian random process, its density function is readily adapted from the literature [14, pp. 287-290]:

$$f_{\hat{\sigma}_Y|\sigma_Y} = (\sigma_Y \sigma_{\hat{\sigma}_Y})^{-1} \hat{\sigma}_Y \left[\phi \left(\frac{\hat{\sigma}_Y^2 - \sigma_Y^2}{2\sigma_{\hat{\sigma}_Y} \sigma_Y} \right) + \phi \left(\frac{\hat{\sigma}_Y^2 + \sigma_Y^2}{2\sigma_{\hat{\sigma}_Y} \sigma_Y} \right) \right] \mu(\hat{\sigma}_Y), \quad (\text{B41})$$

where $\sigma_{\hat{\sigma}_Y}$ is given by Eq. (B38), $\mu(\cdot)$ is the unit-step function, and $\phi(\cdot)$ is defined as

$$\phi(\chi) = (2\pi)^{-1/2} \exp(-\chi^2/2). \quad (\text{B42})$$

Since

$$\phi \left(\frac{\hat{\sigma}_Y^2 + \sigma_Y^2}{2\sigma_{\hat{\sigma}_Y} \sigma_Y} \right) \leq \phi \left(\frac{\sigma_Y}{2\sigma_{\hat{\sigma}_Y}} \right) \quad (\text{B43})$$

for all values of $\hat{\sigma}_Y$, it follows from Eq. (B6) that the second term within the brackets on the right-hand side of Eq. (B41) contributes negligibly to $f_{\hat{\sigma}_Y}$, so that

$$f_{\hat{\sigma}_Y|\sigma_Y} \cong (\sigma_{\hat{\sigma}_Y} \sigma_Y)^{-1} \hat{\sigma}_Y \phi \left(\frac{\hat{\sigma}_Y^2 - \sigma_Y^2}{2\sigma_{\hat{\sigma}_Y} \sigma_Y} \right) \mu(\hat{\sigma}_Y). \quad (\text{B44})$$

Taking the natural logarithm of Eq. (B44) and then the second partial derivative with respect to σ_Y , we obtain

$$-\partial_{\sigma_Y, \sigma_Y}^2 (\ln f_{\hat{\sigma}_Y|\sigma_Y}) = (2\sigma_{\hat{\sigma}_Y})^{-2} [1 + 3(\hat{\sigma}_Y/\sigma_Y)^4]. \quad (\text{B45})$$

Also it can be shown from Eq. (B44) that

$$E\{(\hat{\sigma}_Y/\sigma_Y)^4\} \cong 1, \quad (\text{B46})$$

to the same order of approximation as in Eq. (C27).

From Eqs. (B40), (B45), and (B46)

$$\sigma_{\hat{\sigma}_Y}^2 = \sigma_{\hat{\sigma}_Y}^2 = e^2 \Delta f \Delta f_0. \quad (\text{B47})$$

Since the mean-square estimation error $\sigma_{\hat{\sigma}_Y}^2$ is equal to the Cramér-Rao lower bound, the Fig. B1 processor is a generator of "efficient" estimates for σ_Y .

Appendix C SQUARE ROOT OF A GAUSSIAN RANDOM PROCESS

INTRODUCTION

Our purpose in this appendix is to derive simple expressions for the mean and variance of the square root $B(t)$ of a Gaussian random process $A(t)$ (Fig. 6). The mean and variance of $A(t)$ are called $m_A(t)$ and $\sigma_A^2(t)$ respectively. The mean and variance of $B(t)$ are called $m_B(t)$ and $\sigma_B^2(t)$ respectively.

We will derive the relationships

$$m_B(t) \cong m_A^{1/2}(t) \quad (C1)$$

and

$$\sigma_B(t)/m_B(t) \cong \frac{1}{2} [\sigma_A(t)/m_A(t)], \quad (C2)$$

subject to the assumption that

$$\sigma_A(t)/m_A(t) \ll 1. \quad (C3)$$

The validity of Eq. (C3) is assured in that the process $A(t)$ is the output of a background-limited (BLIP) infrared sensor, for which

$$\sigma_A^2 = 2e\Delta f_0 m_A, \quad (C4)$$

where e is the electronic charge and Δf_0 is the noise bandwidth (Eq. (25)) of the filter $H_0(f)$ (Fig. 6). Although Eq. (C4) is only approximately correct for time-varying $m_A(t)$ (as we will see from Eq. (108)), it can be used to provide an order-of-magnitude estimate for σ_A/m_A . We assume for illustrative purposes that

$$m_A = 10^{-9} \text{ A} \quad (C5a)$$

and

$$\Delta f_0 = 2500 \text{ Hz.} \quad (C5b)$$

It follows from Eqs. (C4) and (C5) that

$$\sigma_A/m_A = O(10^{-3}), \quad (C6)$$

justifying Eq. (C3).

MATHEMATICAL PRELIMINARIES

We write the probability density function of $A(t)$ as

$$f_A(a) = \sigma_A^{-1} \phi \left(\frac{a - m_A}{\sigma_A} \right), \quad (C7)$$

where we define $\phi(\cdot)$ as the normalized Gaussian density:

$$\phi(x) \equiv (2\pi)^{-1/2} \exp(-x^2/2). \quad (C8)$$

Since

$$B(t) = |A(t)|^{1/2}, \quad (C9)$$

it follows from Eq. (C7) that

$$m_B = \sigma_A^{-1} \int_{-\infty}^{\infty} |a|^{1/2} \phi\left(\frac{a - m_A}{\sigma_A}\right) da. \quad (C10)$$

Also,

$$\sigma_B^2 = E\{B^2\} - m_B^2, \quad (C11)$$

where $E\{\cdot\}$ is the statistical expectation operator and

$$E\{B^2\} = \sigma_A^{-1} \int_{-\infty}^{\infty} |a| \phi\left(\frac{a - m_A}{\sigma_A}\right) da. \quad (C12)$$

We devote the remainder of this appendix to developing estimates for Eqs. (C10) and (C12).

EVALUATION OF $E\{B^2\}$

We now write Eq. (C12) as

$$E\{B^2\} = I_1 + I_2, \quad (C13)$$

where

$$I_1 \equiv \sigma_A^{-1} \int_0^{\infty} a \phi\left(\frac{a - m_A}{\sigma_A}\right) da \quad (C14)$$

and

$$I_2 \equiv \sigma_A^{-1} \int_0^{\infty} a \phi\left(\frac{a + m_A}{\sigma_A}\right) da. \quad (C15)$$

Moreover we write Eq. (C14) as

$$I_1 = I_{11} + I_{12}, \quad (C16)$$

where

$$I_{11} \equiv \sigma_A^{-1} \int_{-\infty}^{\infty} a \phi\left(\frac{a - m_A}{\sigma_A}\right) da = m_A \quad (C17)$$

and

$$I_{12} \equiv \sigma_A^{-1} \int_0^{\infty} a \phi\left(\frac{a + m_A}{\sigma_A}\right) da = I_2. \quad (C18)$$

From Eqs. (C13), (C16), (C17), and (C18)

$$E\{B^2\} = m_A + 2I_2, \quad (C19)$$

where I_2 is given by Eq. (C15).

We now write Eq. (C15) as

$$I_2 = \sigma_A^{-1} \int_0^\infty a \phi(a/\sigma_A) g(a) da, \quad (C20)$$

where by definition

$$g(a) \equiv \phi\left(\frac{a + m_A}{\sigma_A}\right) / \phi\left(\frac{a}{\sigma_A}\right). \quad (C21)$$

It can be shown that

$$\max_{0 < a < \infty} g(a) = g(0) = (2\pi)^{1/2} \phi(m_A/\sigma_A). \quad (C22)$$

From Eqs. (C20) and (C22)

$$I_2 < \sigma_A^{-1} (2\pi)^{1/2} \phi(m_A/\sigma_A) \int_0^\infty a \phi(a/\sigma_A) da. \quad (C23)$$

Since the integral in Eq. (C23) evaluates exactly as σ_A^2 , it follows that

$$I_2 < (2\pi)^{1/2} \sigma_A \phi(m_A/\sigma_A). \quad (C24)$$

From Eqs. (C19) and (C24)

$$E\{B^2\} = m_A(1 + \epsilon_A), \quad (C25)$$

where

$$\epsilon_A < 2(2\pi)^{1/2} \left(\frac{\sigma_A}{m_A}\right) \phi\left(\frac{m_A}{\sigma_A}\right). \quad (C26)$$

It follows from Eqs. (C6), (C25), and (C26) that the quantity ϵ_A is truly negligible and that to all intents

$$E\{B^2\} = m_A. \quad (C27)$$

EVALUATION OF m_B

We now write Eq. (C10) as

$$m_B = I_3 + I_4, \quad (C28)$$

where

$$I_3 \equiv \sigma_A^{-1} \int_0^\infty a^{1/2} \phi\left(\frac{a - m_A}{\sigma_A}\right) da, \quad (C29)$$

and

$$I_4 \equiv \sigma_A^{-1} \int_0^\infty a^{1/2} \phi\left(\frac{a + m_A}{\sigma_A}\right) da. \quad (C30)$$

Equation (C30) can be estimated by means similar to those used in estimating Eq. (C15) to obtain the bound

$$I_4 < m_A^{1/2} \left[\frac{\sqrt{\pi}}{2} \left(\frac{\sigma_A}{m_A}\right)^2 \phi\left(\frac{m_A}{\sigma_A}\right) \right]. \quad (C31)$$

It follows from Eqs. (C6) and (C31) that

$$I_4 = 0, \quad (C32)$$

to the same order of approximation as Eq. (C27).

The first step in evaluating I_3 is to write Eq. (C29) as

$$I_3 = m_A^{1/2} \int_{-(m_A/\sigma_A)}^{\infty} \left[1 + \left(\frac{\sigma_A}{m_A} \right) u \right]^{1/2} \phi(u) du. \quad (C33)$$

Writing a binomial expansion for the square root of the bracketed quantity in Eq. (C33), we obtain

$$I_3 = m_A^{1/2} \left[I_{30} + \frac{1}{2} \left(\frac{\sigma_A}{m_A} \right) I_{31} - \frac{1}{8} \left(\frac{\sigma_A}{m_A} \right)^2 I_{32} + \dots \right], \quad (C34)$$

where

$$I_{3j} \equiv \int_{-(m_A/\sigma_A)}^{\infty} u^j \phi(u) du, \quad j = 1, 2, 3. \quad (C35)$$

It can be shown from Eqs. (C6) and (C35) that

$$I_{30} = I_{32} = 1 \quad (C36)$$

and

$$I_{31} = 0 \quad (C37)$$

to the same order of approximation as Eqs. (C27) and (C32).

From Eqs. (C28), (C32), (C34), (C36), and (C37)

$$m_B = m_A^{1/2} \left[1 - \frac{1}{8} \left(\frac{\sigma_A}{m_A} \right)^2 \right]. \quad (C38)$$

From Eqs. (C11), (C27), and (C38)

$$\sigma_B^2 \cong m_A \left(\frac{\sigma_A}{2m_A} \right)^2 = \frac{\sigma_A^2}{4m_A}. \quad (C39)$$

From Eqs. (C6), (C38), and (C39)

$$m_B = m_A^{1/2} (1 - \epsilon) \quad (C40)$$

and

$$\sigma_B/m_B = \frac{1}{2} (\sigma_A/m_A) (1 + \epsilon), \quad (C41)$$

where

$$\epsilon = \frac{1}{2} (\sigma_A/2m_A)^2 = O(10^{-6}). \quad (C42)$$

Thus, Eqs. (C1) and (C2) have been validated, and the relative errors have been estimated.

Finally from Eqs. (C4) and (C39)

$$\sigma_B^2 = \frac{2e\Delta f_0 m_A}{4m_A} = e\Delta f_0/2. \quad (C43)$$

It is interesting to compare Eqs. (C4) and (C43). According to Eq. (C4) the noise at the input to the square-root device is a function of m_A (and hence the mean photon flux incident on the detector). However, Eq. (C43) indicates that the noise at the output of the square-root device is independent of the mean photon flux.

REFERENCES

1. R.A. Steinberg, "Passive Infrared Surveillance, Part I: Model Formulation," NRL Report 8320, Sept. 28, 1979.
2. R.A. Steinberg, "Passive Infrared Surveillance with Background-Limited Sensors: New Methods of Analysis," NRL Memorandum Report 4078, Sept. 24, 1979.
3. D.Z. Robinson, "Methods of Background Description and their Utility," Proc. IRE **47**:1554 (1959).
4. H.L. Van Trees, *Detection, Estimation, and Modulation Theory, Part I*, Wiley, New York, 1968.
5. G.V. Trunk, "Survey of Radar Signal Processing," NRL Report 8117, June 21, 1977.
6. R.M. Gagliardi and S. Karp, *Optical Communications*, Wiley, New York, 1976.
7. W.K. Pratt, *Laser Communication Systems*, Wiley, New York, 1969.
8. S.O. Rice, "Mathematical Analysis of Random Noise," in *Selected Papers on Noise and Stochastic Processes*, edited by N. Wax, Dover, New York, 1954.
9. *Electro-Optics Handbook*, RCA, Burlington, Mass., 1968.
10. K. Seyrafi, *Electro-Optical Systems Analysis*, Electro-Optical Research Company, Los Angeles, 1973.
11. J.M. Lloyd, *Thermal Imaging Systems*, Plenum, New York, 1975.
12. I.R. Able, "Radiometric Accuracy in a Forward Looking Infrared System," Optical Engineering **16**:241, May-June 1977.
13. J.W. Goodman, *Introduction to Fourier Optics*, McGraw-Hill, New York, 1968.
14. J.B. Thomas, *An Introduction to Statistical Communication Theory*, Wiley, New York, 1969.
15. A.F. Milton, "Charge Transfer Devices for Infrared Imaging," in *Topics in Applied Physics, Vol. 19: Optical and Infrared Detectors*, edited by R.J. Keyes, Springer-Verlag, Berlin, 1977.

